RSC Advances

PAPER

View Article Online
View Journal | View Issue

Check for updates

Cite this: *RSC Adv.*, 2020, **10**, 25567

Glauconite clay-functionalized chitosan nanocomposites for efficient adsorptive removal of fluoride ions from polluted aqueous solutions

Marwa M. Sobeih,[ab] M. F. El-Shahat,*[a] A. Osman,[c] M. A. Zaid[b] and Mostafa Y. Nassar *[d]

Received 12th March 2020
Accepted 25th June 2020

DOI: 10.1039/d0ra02340j

rsc.li/rsc-advances

We herein have developed a mild approach for the fabrication of glauconite clay (G)-modified chitosan (CS) nanocomposites by the combination of a simple blending and crosslinking method. The chitosan was modified with ethylenediaminetetraacetic acid (EDTA), glutaraldehyde (GL), sodium dodecyl sulfate (SDS), and cetyltrimethyl ammonium bromide (CTAB). The as-prepared composites were identified using Fourier-transform infrared spectroscopy (FTIR), X-ray diffraction (XRD), field emission scanning electron microscopy (FE-SEM), nitrogen physical adsorption (BET), atomic absorption spectrophotometry (AA), and thermal gravimetric analysis (TGA). The adsorption activities of the as-prepared materials were assessed for the removal of fluoride ions from aqueous media using a batch technique. Raw glauconite (G), GL-CS/G, SDS-CS/G, EDTA-GL-CS/G, and CTAB-CS/G adsorbents displayed maximum adsorption capacity values of 1.15, 4.31, 4.55, 6.90, and 9.03 mg g^{-1}, respectively. The adsorption results were well described by employing the pseudo-second-order kinetic and Langmuir isotherm models. The estimated thermodynamic constants indicated that the F^- ion adsorption was a spontaneous, physisorption process. Furthermore, the modified chitosan adsorbents are good candidates for the adsorptive elimination of F^- ions from aqueous solutions, according to their reusability, high stability, good adsorption capacity, and applicability for actual field water samples.

1 Introduction

Although fluoride ions (F^-) are identified as a crucial component for the normal functioning of the human body such as the formation and preservation of teeth, regular consumption of fluoride ions beyond recommended levels brings about various health issues. For example, the excessive intake of fluoride can cause dental and skeletal fluorosis as well as fluoride ousting in bone which can cause structural damage in ligaments.[1] The anthropogenic fluoride is the most frequent type and its occurrence is attributed to waste discharging from several industries into the environment.[2] After guidance from the WHO, various countries agreed to set 1.5 mg L^{-1} of fluoride concentration as the maximum contaminant level of that species in drinking waters.[2]

So far, numerous physical and chemical means have been applied to remove fluoride ions from polluted waters, such as coagulation,[3] precipitation,[4] electro-coagulation (EC),[5] solar distillation,[6] adsorption, and ion-exchange methods.[7] Among these procedures, adsorption is still the most suitable process because it is simple and offers low-cost performance.[8,9] Various commercial adsorbents such as charcoal, fly ash,[10] activated alumina, activated carbon, groundnut husk,[11] and zeolite[12] are employed for fluoride adsorption from water. However, most of those adsorbents have some shortcomings due to their low performance and high-cost production. Accordingly, natural materials such as clays and zeolites have received a notable attention due to their local availability, chemical and mechanical stability, low-cost production, good adsorption capacities, and layered structure.[13]

Besides, heterogeneous phyllosilicate mineral sediments with a chemical formula of $(K,Na)(Fe,Al,Mg)_2(Si,Al)_4O_{10}(OH)_2$ are recognized as glauconite clay (G), green clay, green sand or green earth, and they have a bluish-green to greenish-black color.[14] This clay has a structure of one di-octahedral layer sandwiched between two silicon tetrahedral layers in the presence of alumina and silica together with relatively high iron- and potassium oxides.[15] More studies showed that glauconite clay has been widely used as a preferred adsorbent in water treatment applications for the removal of different metal ions and dyes.[16] The adsorption capacities of clays can be enhanced by their modification using some polymers such as chitosan.[17]

---

[a] Chemistry Department, Faculty of Science, Ain Shams University, Cairo, Egypt. E-mail: elshahatmf@hotmail.com; Tel: +20 1128323115

[b] Abu-Zaabal Company for Fertilizer and Chemical Company (AZFC), EL-Qalyubia, Egypt

[c] Geology Department, Faculty of Science, Ain Shams University, Cairo, Egypt

[d] Chemistry Department, Faculty of Science, Benha University, Benha 13815, Egypt. E-mail: m_y_nassar@yahoo.com; m_y_nassar@fsc.bu.edu.eg; Tel: +20 1068727555

Chitosan is a good candidate polymer, owing to its low cost, local availability, biocompatibility, biodegradability, non-toxicity, bioactivity, as well as its great number of hydroxyl and amine groups.[18] The chemical stability of this polymer can be reinforced through treatments using functional crosslinking agents. However, most of the cross-linkers reduce the adsorption efficiency of chitosan in most cases, owing to the involvement of the amino groups in the crosslinking procedure. Consequently, the introduction of special functional groups such as amino, sulfur, carboxyl, and alky groups into the polymeric matrix of chitosan is an effective way to enhance the adsorption capacity and selectivity of the adsorbents.[19] This can be performed by using ethylenediaminetetraacetic acid (EDTA), which improves the adsorption capacities of the adsorbents.[20] Furthermore, chitosan modification utilizing surfactants such as sodium dodecyl sulfate (SDS) and cetyltrimethyl-ammonium bromide (CTAB) not only overcomes the challenge of high agglomeration but also makes adsorbents with good adsorption capacity, selectivity, and high stability.[21]

However, the fabrication of most of the earlier reported adsorbents was multi-step and/or time-consuming. The synthesis of adsorbents with low-cost production, good recyclability, and high adsorption capacity is still deeply favored. The fabrication of glauconite clay and EDTA, surfactant-modified chitosan composites and applying them for the elimination of fluoride ions have not been reported, so far. Accordingly, herein, we have developed a new strategy to fabricate cross-linked chitosan/glauconite clay, EDTA-chitosan modified glauconite, CTAB-modified chitosan/glauconite, and SDS-modified chitosan/glauconite composites employing a simple approach. The adsorption properties of the as-synthesized glauconite clay adsorbents were examined for the elimination of fluoride ions from aqueous media. The impact of some parameters on the adsorption process was further explored. The as-prepared adsorbents were identified utilizing various means.

2 Experimental

2.1. Materials and reagents

Glauconite clay (G) was collected from the El-Gideda area, Bahariya Oasis, located in the central section of the western desert, 370 km southwest of Cairo, Egypt. Chitosan (CS) (degree of deacetylation >85%), sodium dodecyl sulfate (SDS), and cetyltrimethyl ammonium bromide (CTAB) were obtained from Sigma Chemical Co., USA. All other chemicals were of analytical grade. Acetic acid, sodium hydroxide, HCl, and glutaraldehyde (GL) were used without additional purification as obtained from El-Nasr Pharmaceutical Chemicals Company (ADWIC)-Company, Egypt. The standard stock solution (1000 mg L^{-1}) of fluoride was prepared by dissolving 2.21 g of sodium fluoride (Merck, Germany) in one liter of de-ionized water. Then, the required fluoride solution concentration was prepared by successive dilution of the stock solution. The desired pH was regulated by using 0.2 M HCl and/or NaOH solutions. De-ionized water was used for all reagent solutions. For the field study, water containing fluoride was collected from wastewater ponds in Abu-Zaabal for Fertilizers and Chemicals Company (AZFC), Egypt. Collection and samples preservation for the pH, turbidity, and COD were done according to the standard methods for the examination of water and wastewater.[22]

2.2. Adsorbents formation

2.2.1. Glauconite clay (G). The glauconite clay (G) sample was washed with distilled water several times with constant stirring to remove soluble inorganic salts and any adhering substances. The sample was allowed to settle, separated from the liquid by filtration, and dried at 100 °C until a constant weight was attained. The dried G product was sieved into different grain size fractions: <63, 63–125, 125–250, 250–500, 500–800, and 800–1000 μm. The glauconite clay (G) of a grain size fraction of 125–500 μm was selected for the adsorption study.

2.2.2. Formation of cross-linked chitosan/glauconite clay (GL-CS/G) composite. A chitosan solution was prepared by dissolving 1 g chitosan powder in 100 mL of (2%,v/v) acetic acid solution, having 1 g natural glauconite clay (G), and the reaction system was maintained agitating for 2 h at *ca.* 25 °C. Afterward, the cross-linking method was carried out *in situ* by the addition of 1 mL glutaraldehyde (GL) as a cross-linker to the previously stirring blend. The stirring was extended for 23 h at 60 °C, the generated gel was washed with distilled water to eliminate any free GL, then dried at 60 °C.[23] Eventually, the dried cross-linked chitosan-glauconite clay (GL-CS/G) composite was crushed and sieved, to get a particle size of 80–100 mesh to ensure the sufficient surface area for adsorption.

2.2.3. Formation of EDTA-chitosan modified glauconite (EDTA-GL-CS/G) composite. EDTA-modified chitosan was prepared according to the reported method with some modification.[24] The EDTA-modified chitosan was *in situ* prepared in the presence of natural glauconite as following: 1 g chitosan powder was dissolved in (2%,v/v) acetic acid solution (100 mL), having 1 g natural glauconite clay (G), and the reaction system was continued stirring overnight. Afterward, 1 mL of glutaraldehyde (GL) and 50 mL of 0.2 M EDTA, adjusted with NaOH solution at pH 8.5, were then also added to the reaction mixture, forming a gel product. The generated gel was filtered, washed with deionized water to remove unreacted EDTA, and then dried at 60 °C. Lastly, the dried EDTA-GL-CS/G composite was ground and saved for further usage.

2.2.4. Formation of surfactant-modified chitosan/glauconite (CTAB-CS/G and SDS-CS/G) composite. Surfactant-modified chitosan was fabricated based on the reported procedure with some modification.[25] The surfactant-modified chitosan was *in situ* fabricated in the presence of natural glauconite as following: 1 g chitosan was dissolved in (2%,v/v) acetic acid solution (100 mL), containing 1 g natural glauconite clay (G), and the reaction mixture was allowed to stir overnight. On the other hand, a coagulating blend ($H_2O : CH_3OH : NaOH$: 4 : 5 : 1, w/w) was prepared. Next, the previously prepared chitosan solution was added drop wise to the coagulating mixture using a micropipette (5 mL capacity). Spherical and uniform beads were generated attributing to the neutralization of acetic acid present in the CS gel by the action of the alkaline coagulating mixture. After that, the prepared chitosan beads were left settled overnight and rinsed with deionized water. The resulting beads were immersed in surfactant solutions; SDS or CTAB (0.6 g SDS or CTAB dissolved in 100 mL deionized water), to form CTAB-CS/G and SDS-CS/G composites, respectively. The beads were left undisturbed for 3 days at room temperature (*ca.* 25 °C ± 2), and then separated. The prepared surfactant-modified chitosan beads were washed with deionized water and preserved in deionized water for future usage.

2.3. Materials characterization

Characterization of raw glauconite and its composites were carried out utilizing X-ray diffraction (XRD): X-ray diffractometer model X'Pert PRO with Cu-radiation ($\lambda = 1.542$ Å) source operated at 45 kV and 35 mA with scanning speed of 0.02° s^{-1}. The information about the changes occurring in the structure of G before and after modification was determined by FT-IR spectra. The FT-IR spectra were obtained with an FTIR Spectrometer (Shimadzu 4100) in the transmittance (%) mode with a scan resolution of 4 cm^{-1} in the range of 4000 to 400 cm^{-1}, using KBr pellets. A thermal gravimetric analysis (TGA) was collected on a thermal analyzer instrument (Shimadzu; model TA-60WS) in 27–800 °C temperature range with 15 °C min^{-1} heating rate under nitrogen gas atmosphere. The morphology of raw and the as-fabricated products was investigated utilizing a Quanta, FEI Quanta model FEG 250 scanning electron microscopy (FEI Company, USA) with an excitation voltage of 20 kV. The specific surface area studies of raw and modified chitosan/clay composites were performed using BET (Brunauer, Emmett and Teller) method after N_2 adsorption–desorption using Quantachrome (USA; Nova 2000 series) analyzer. The UV-Vis spectra of adsorption studies were taken utilizing a Jasco UV-Vis spectrophotometer. Where the fluoride ion concentration was determined by alizarine fluorine blue method and the absorbance of the formed complex was evaluated at 625 nm, according to the reported method.[26] The chemical compositions of the glauconite and its modified forms were estimated employing an atomic absorption spectrophotometer (Unicam, Solar 929, UK supplied with acetylene and nitrous oxide burner heads). A Janway flame-photometer, Germany, was utilized for sodium and potassium estimation.

2.4. Adsorption studies

Various batch experiments were performed to estimate the efficiency of the bare glauconite clay and its prepared composites, as adsorbents, for the elimination of fluoride ions from contaminated aqueous solutions. In a typical batch procedure: 0.1 g adsorbent was magnetically stirred (350 rpm stirring speed) in 50 mL of the fluoride solution of a particular initial concentration (C_0, mg L^{-1}) at 25 °C temperature, and particular pH value. It is worthy to mention that the pH of the adsorption media was first set to the necessary pH value utilizing HCl and/or NaOH aqueous solutions (0.2 M), and the adsorbent was then added. After adsorption, at pre-defined time intervals, aliquots of the adsorption solution were taken outside the flask and centrifuged to isolate the adsorbent. The residual fluoride concentration in the supernatant was determined by a UV-Vis spectrophotometer utilizing a pre-constructed calibration curve for that anion. We calculated the percent removal efficiency (R%), adsorption capacity (q_t, mg g^{-1}) of the adsorbent, and the equilibrium adsorption capacity (q_e, mg g^{-1}) of the adsorbent applying eqn (1), (2), and (3), respectively.

$$R\% = [(C_0 - C_t)/C_0] \times 100 \tag{1}$$

$$q_t = V(C_0 - C_t)/m \tag{2}$$

$$q_e = V(C_0 - C_e)/m \tag{3}$$

where C_0 (mg L^{-1}), C_t (mg L^{-1}), and C_e (mg L^{-1}) are the initial fluoride concentration, fluoride concentration, and equilibrium fluoride concentration at time 0, t, and equilibrium time, respectively, for the adsorption. Besides, V (L) is fluoride solution volume and m (g) is mass of the adsorbent. Moreover, we explored various parameters controlling the fluoride ion adsorption such as contact time, pH, initial fluoride concentration, and temperature.

3 Results and discussion

3.1. Characterization of glauconite clay and its fabricated composites

3.1.1. Chemical analysis of raw glauconite clay. The chemical composition of glauconite clay (G) is provided in Table 1. The chemical analysis showed that G is essentially composed of SiO_2 (50.50%), Fe_2O_3 (20.88%), Al_2O_3 (7.88%) and K_2O (5.00%) as major components. The ratios of SiO_2 to Al_2O_3 and SiO_2 to Fe_2O_3 are *ca.* 6.4, 2.41, respectively. Glauconite clay (G) contains also exchangeable cations that play a vital function in F^- ion uptake throughout the de-fluorination process such as Na^+, K^+, and Ca^{2+}.[27] These results confirm the aluminosilicate structure of G clay that supports its application as a reliable sorbent for F^- ion. Other physical features such as bulk density, specific surface area and moisture content were determined based on appropriate standards[28] and found to be 1.35 g cm^{-3}, 47.59 m^2 g^{-1} and 4.62%, respectively. According to the sieve analysis, the grain size fractions: <63 μm, 125–63 μm, and 500–125 μm constituted 1.48%, 2.67%, and 87.33%, respectively of

Table 1 Chemical composition of glauconite clay (G) mineral

Constituent	Content (wt%)
SiO_2	50.50
Al_2O_3	7.88
Fe_2O_3	20.88
MgO	2.81
CaO	0.34
P_2O_5	0.38
K_2O	5.00
SO_3	1.2
Na_2O	0.95
Loss-on-ignition	9.70

the total weighted mass of the G sample. Smaller quantity was constituted for size fraction of 800–500 μm that was *ca.* 0.34%, while the grain size fraction of 800–1000 μm constituted 8.18% of the total weighted mass of the sample. G grains with size fraction of 500 to 125 μm was selected for this investigation because it constituted *ca.* 87.33% of the total mass of the adsorbent sample. This selection was in line with the reported results,[29] which confirmed that grains of 100–500 μm size are typically homogeneously glauconitized compared to other size fractions.

3.1.2. XRD study. Fig. 1(a–e) displays the XRD patterns of G, GL-CS/G, EDTA-GL-CS/G, SDS-CS/G, and CTAB-CS/G adsorbents, respectively. The X-ray diffraction pattern of G clay (Fig. 1(a)) showed explicitly that the predominant peaks are due to different phases like illite, smectite, and dolomite with the predominance of the quartz phase. Such a composition of G clay is in good consistency with glauconite term in a mineralogical thought to indicate a Fe-rich illite-smectite clay mineral.[30] On the other hand, XRD patterns of GL-CS/G, EDTA-GL-CS/G, SDS-CS/G, and CTAB-CS/G composites (Fig. 1(b–e)) manifested a typical peak at $2\theta = 20.13°$ characteristic for chitosan along with the diffraction peaks for G clay. The low intensity of this peak is probably owing to hydrogen bonding and cross-linking of the chitosan.[31] The XRD patterns of all prepared composites manifested the characteristic reflection peaks for G sample. Moreover, the XRD pattern of GL-CS/G showed a slight shifting to lower angle compared to that of raw G with a decrease in the peaks intensity, revealing the incorporation of chitosan into G interlayer spaces. Also, the disappearance of distinctive crystalline peak of chitosan around $2\theta = 10.00°$, may be due to the destruction of the intermolecular hydrogen bonds and the chitosan crystallinity caused by the interaction of G with chitosan. The diffraction pattern of EDTA-GL-CS/G (Fig. 1(c)) showed an additional diffraction peak at $2\theta = 18.32°$, indicating the presence of EDTA.[23] In addition to the diffraction peak appeared at $2\theta = 20.13°$ characteristic for chitosan, the XRD pattern (Fig. 1 (d)) for SDS-CS/G displayed also some reflection peaks at $2\theta = 18.36°$, 20.81°, and 21.86°, due to the co-existence of SDS in the SDS-CS/G composite along with chitosan and G clay.[32] The XRD pattern (Fig. 1(e)) of CTAB-CS/G composite also revealed the diffraction peaks of G with a small shifting at $2\theta =$ 20°, 35°, and 62°, owing to binding of G with chitosan. No remarkable change in the XRD pattern of G sample was recognized after CTAB-CS/G formation, indicating that the crystal structure of G was retained in composite.[33] However, other peaks at $2\theta = 27°$ and 29° are observed, which can be ascribed to the traces of quartz and kaolinite minerals.

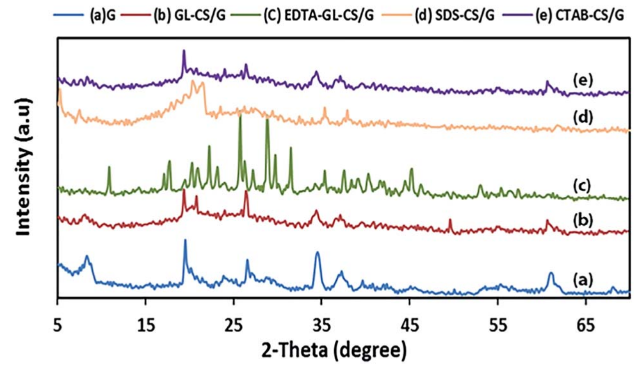

Fig. 1 XRD patterns of G (a), GL-CS/G (b), EDTA-GL-CS/G (c), SDS-CS/G (d), and CTAB-CS/G (e) products.

3.1.3. FT-IR study. The chemical structures of G, GL-CS/G, EDTA-GL-CS/G, SDS-CS/G, and CTAB-CS/G adsorbents were analyzed by utilizing FT-IR spectroscopy in range 4000 to 400 cm^{-1}. The FT-IR spectrum (Fig. 2(a)) of G clay showed absorption bands at *ca.* 3494 and 1629 cm^{-1} due to the stretching and bending vibrations of –OH groups of adsorbed water molecules and metal hydroxides that G clay has.[34,35] The spectrum showed also vibrational bands at *ca.* 819 and 1014 cm^{-1}, attributing to Fe–OH bending and Si(Al)–O–Si asymmetric stretching, respectively.[8,35,36] The bending vibration of Si–O bond appeared at *ca.* 673 cm^{-1}. The vibrational frequencies appeared at *ca.* 435, 447 and 497 cm^{-1} are correlated to Si–O–Mg, Si–O–Si, and Si–O–Fe^{3+} bending vibrations, respectively.[37] On the other hand, FT-IR spectra (Fig. 2) of GL-CS/G, EDTA-GL-CS/G, SDS-CS/G, and CTAB-CS/G composites showed two bands at about 1620 and 3450 cm^{-1} corresponding to O–H bending and stretching frequencies of adsorbed water molecules and metal hydroxides, indicating the formation of the hydrogen bonds in all different composites.[38] These bands are shifted to low frequencies comparing to those of the pristine G clay.

Furthermore, the two vibrational bands which appeared at 435 and 447 cm^{-1} for pristine G clay were shifted to higher frequencies for the prepared composites. Vibrations of silica group comprising of Si–O–Si bend and Si–O–Si symmetric and asymmetric stretches were appeared at lower frequencies for the prepared composites compared to the G clay.[35] These bands

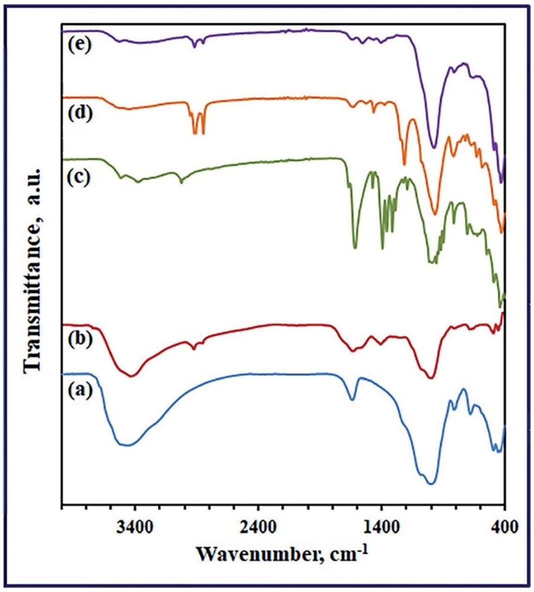

Fig. 2 FT-IR spectra of G (a), GL-CS/G (b), EDTA-GL-CS/G (c), SDS-CS/G (d), and CTAB-CS/G (e) products.

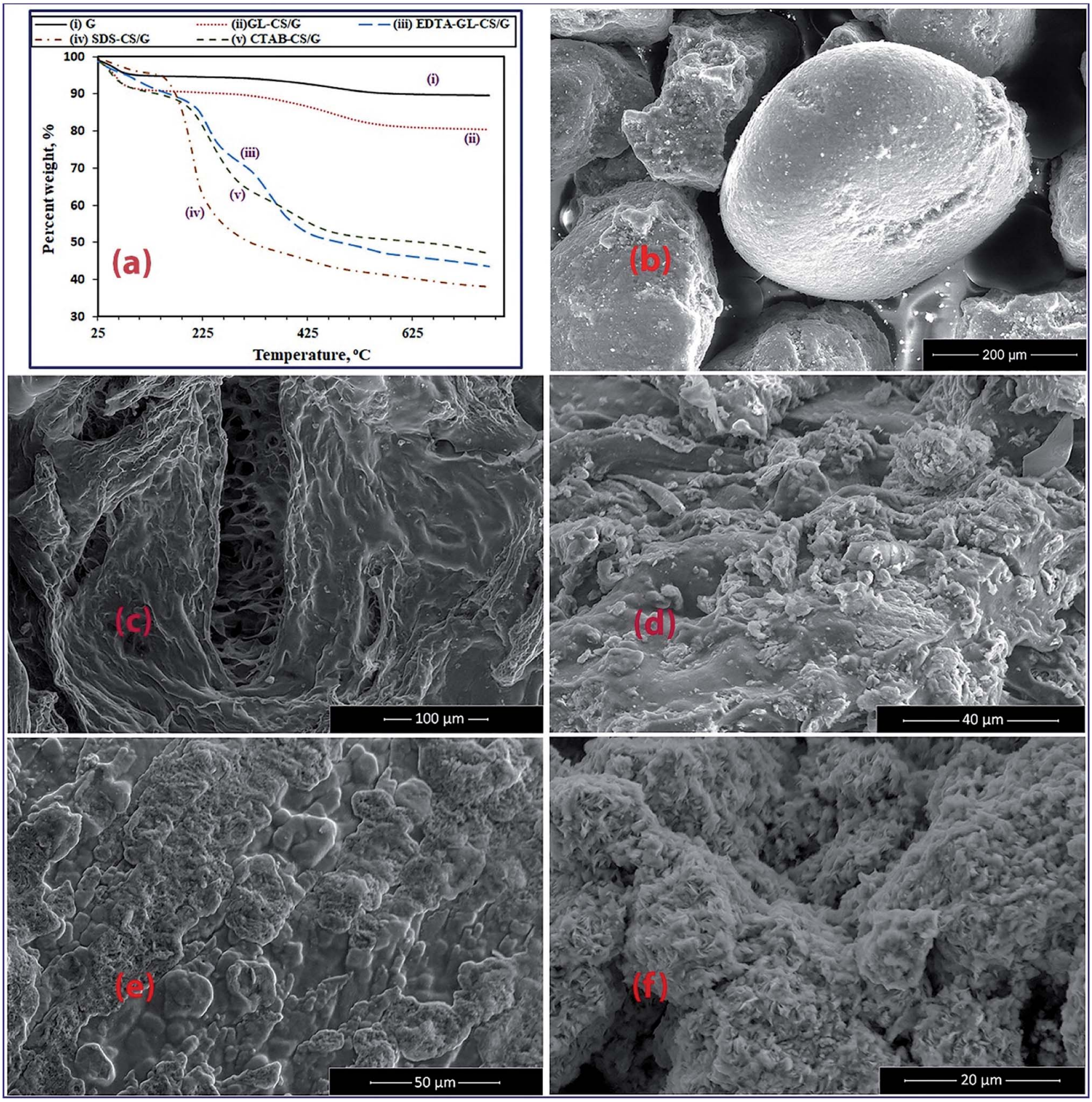

Fig. 3 TG analyses for the products (a); and FE-SEM images for G (b), GL-CS/G (c), EDTA-GL-CS/G (d), SDS-CS/G (e), and CTAB-CS/G (f) products.

appeared at *ca.* 804 and 989; 815 and 988; 970; as well as 809 and 970 cm^{-1} for GL-CS/G, EDTA-GL-CS/G, SDS-CS/G, and CTAB-CS/G composites, respectively. It is clearly seen that all the prepared chitosan/clay composites exhibited the characteristic bands assigning to $-NH_2$ and –OH groups in the frequency range of 3400–3500 cm^{-1}. The spectra of the composites exhibited also vibrational bands at 2924, 3007, 2917, and 2919 cm^{-1}, which may be attributed to –CH stretching of chitosan, for composites for GL-CS/G, EDTA-GL-CS/G, SDS-CS/G, and CTAB-CS/G, respectively. The bending vibrational bands due to methylene and methyl groups appeared in the range of 1314–1475 cm^{-1}, for the composites. The vibrational bands appeared at about 1623, 1610, 1629, and 1627 cm^{-1} are probably due to $-C{=}O$ groups for the aforementioned composites, respectively. The bending $-NH_2$ group appeared in the range of 1410–1475 cm^{-1} for the as-prepared composites. The shift in this vibration might be expected when an interaction between functional groups of $-NH_2$ and the clay negatively-charged sites is occurred.[39] The FT-IR spectrum (Fig. 2(c)) of EDTA-GL-CS/G showed also a band at 1666 cm^{-1} corresponding to $-C{=}O$ stretching vibration of the EDTA carboxylate groups. This spectrum showed also vibrational bands in the range of 1319–

1475 cm^{-1}, which are probably due to bending –CH$_2$ groups of the EDTA, indicating successful grafting of EDTA into the composite.[40]

In addition to the aforementioned characteristic vibrations of G clay and chitosan, the FT-IR spectra of the surfactant modified CS/G composites showed also other vibrational bands assigning to the SDS and CTAB surfactants, implying the formation of SDS-CS/G and CTAB-CS/G composites. The FT-IR spectrum (Fig. 2(d)) of SDS-CS/G exhibited vibrational bands at 2950, 2917, and 2850 cm^{-1} due to asymmetric stretching vibration of –CH$_3$, asymmetric stretching vibration of –CH$_2$, and symmetric stretching vibration of –CH$_3$ and –CH$_2$, respectively, of the hydrophobic tail of the SDS molecule.[41] The vibrational bands at *ca.* 1466 and 1374 cm^{-1} can be attributed to a bending vibration of –CH$_2$ and a deformation vibration of –CH$_3$, respectively.[41,42] The characteristic vibrations of the hydrophilic sulfonate head (–OSO$_3$–) of the SDS surfactant appeared in the range of 1003–1250 cm^{-1}. The strong vibrational doublet at *ca.* 1248 and 1218 cm^{-1} is due to asymmetric stretching of S–O bond. Whereas, the absorption bands at 970 and 1070 cm^{-1} are probably contributing to symmetric stretching of S–O bond.[42] These findings support the hydrophobic interaction of the SDS surfactant on the surface of G clay and its impregnation into the interlayer space of clay.[41,43] The FT-IR spectrum (Fig. 2(e)) of CTAB-CS/G featured vibrational frequencies at *ca.* 2919 and 2853 cm^{-1} attributing to asymmetric and symmetric stretching vibrations of –CH$_2$ group respectively. The scissoring vibrations of –CH$_2$ group are observed at *ca.* 1407 and 1458 cm^{-1}. Besides, small bands for the wagging vibrations of –CH$_2$ group appeared in the range of *ca.* 1300–1400 cm^{-1}. Whereas, the hydrophilic headgroup of the CTAB surfactant featured a small band at *ca.* 2956 cm^{-1}, attributing to symmetric stretching of the –N–CH$_3$ groups. These groups showed their asymmetric stretching vibrations as small and broad bands at around 3010 cm^{-1}. While the bending vibration of the –N–CH$_3$ appeared at *ca.* 1374 cm^{-1} and that of –C–N groups appeared as a shoulder at *ca.* 910 cm^{-1}. These findings indicated that the CTAB molecule was impregnated into the interlayer space of the G clay.[44]

3.1.4. Thermal analysis study. The TG analysis was applied to investigate the transformational behavior in above mentioned adsorbents at a heating rate of 10 °C min^{-1} under a nitrogen atmosphere, as depicted in Fig. 3(a)(i–v), respectively. The TG curve of G clay (Fig. 3(a)(i)) revealed a weight loss of about 5.31% in the temperature range of 80–200 °C due to the vaporization of water molecules. Rising the temperature up to 600 °C resulted in an additional loss of water molecules and decomposition of the crystal structure of G (5.34%). On the other hand, all the TG curves (Fig. 3(a)(ii–v)) of synthesized composites exhibited their relatively high thermal stability. This can be attributed to the high thermal stability of G clay that appeared clearly after the interaction between chitosan and clay particles in the synthesized composites. The TG curve (Fig. 3(a)(ii)) of GL-CS/G composite exhibited two stages of weight losses in the temperature ranges below 211 °C with a value of 10%, and above 211 °C with a weight loss equal to 10.1%. The first step is probably attributing to the evaporation of the surface water molecules. The second step may be due to de-polymerization and decomposition of some of the chitosan and GL units of the GL-CS/G composite. This value is not high comparing to the other chitosan composites due to its thermal stability, which is attributing to utilizing GL cross-linker in its preparation. The TG curve of EDTA-GL-CS/G composite (Fig. 3(a)(iii)) showed three weight losses of values 9.14%, 18.96%, and 28.39% in temperature ranges below 200 °C, 228–350 °C, and above 500 °C, respectively. The first weight loss is presumably due to the elimination of the adsorbed surface water molecules. The second weight loss can be returned to de-polymerization and decomposition of the acetylated and de-acetylated units of the adsorbent. The final step is probably owing to the decomposition of EDTA-GL-CS/G adsorbent. The TG curve (Fig. 3(a)(iv)) of SDS-CS/G revealed one main weight loss step of about 62.03% in the temperature range of 40–500 °C, owing to two superimposed stages. This is presumably due to the dehydration of physically adsorbed water from 40 to 200 °C and decomposition of surfactants from 200 to 500 °C. Eventually, the TG curve (Fig. 3(a)(v)) of CTAB-CS/G exhibited three weight loss stages. In the first stage, a slight weight loss of 9.79% was appeared below 200 °C, attributing to the surface water molecules evaporation. The second stage, weight loss of 28.97%, was observed in the temperature range from 250 to 382 °C, due to the decomposition of acetylated and de-acetylated units of adsorbent, which was similar to the EDTA-GL-CS/G adsorbent thermal behavior. Thereafter, a weight loss of 14.29%, over 500 °C, was probably due to the decomposition of the composite. These findings indicated that all the adsorbents of interest have a relatively good thermal stability. This can be explained as the introduction of inorganic components into organic materials can intensify their thermal stability as well as the high thermal stability of G and the interaction between chitosan and the G particles.[45]

3.1.5. Surface morphology and textural structure. The SEM images of G, GL-CS/G, EDTA-GL-CS/G, SDS-CS/G, and CTAB-CS/G adsorbents (Fig. 3(b–f)) revealed significant changes in the surface morphologies of the G sample after different modification processes. The SEM image (Fig. 3(b)) of the G sample exhibited the typical morphology for this mineral, which is regular and irregular spherical grains with presence of small cavities and cracks on their surfaces. Once the cross-linked chitosan/glauconite clay composite has been formed, the SEM image of the GL-CS/G product showed the coverage of the glauconite with cross-linked chitosan rough layered structures (Fig. 3(c)). The SEM image (Fig. 3(d)) of EDTA-GL-CS/G composite exhibited that the composite is composed of sphere-like particles of G clay impeded into rough surface of layered structure of EDTA-GL-CS. Modification of the CS/G composites with SDS surfactant produced more porous, rough, folded, and condensed layered structures with some sphere-like agglomerates, as shown in Fig. 3(e). Whereas, modification of the composite with CTAB surfactant brought about product composed of cotton-like structure with spherical particles, as displayed in Fig. 3(f). Besides, it is clearly seen that CTAB-CS/G product has a highly porous structure.

To get more insight into the surface structures of the products, the porosity and BET surface areas of the products were

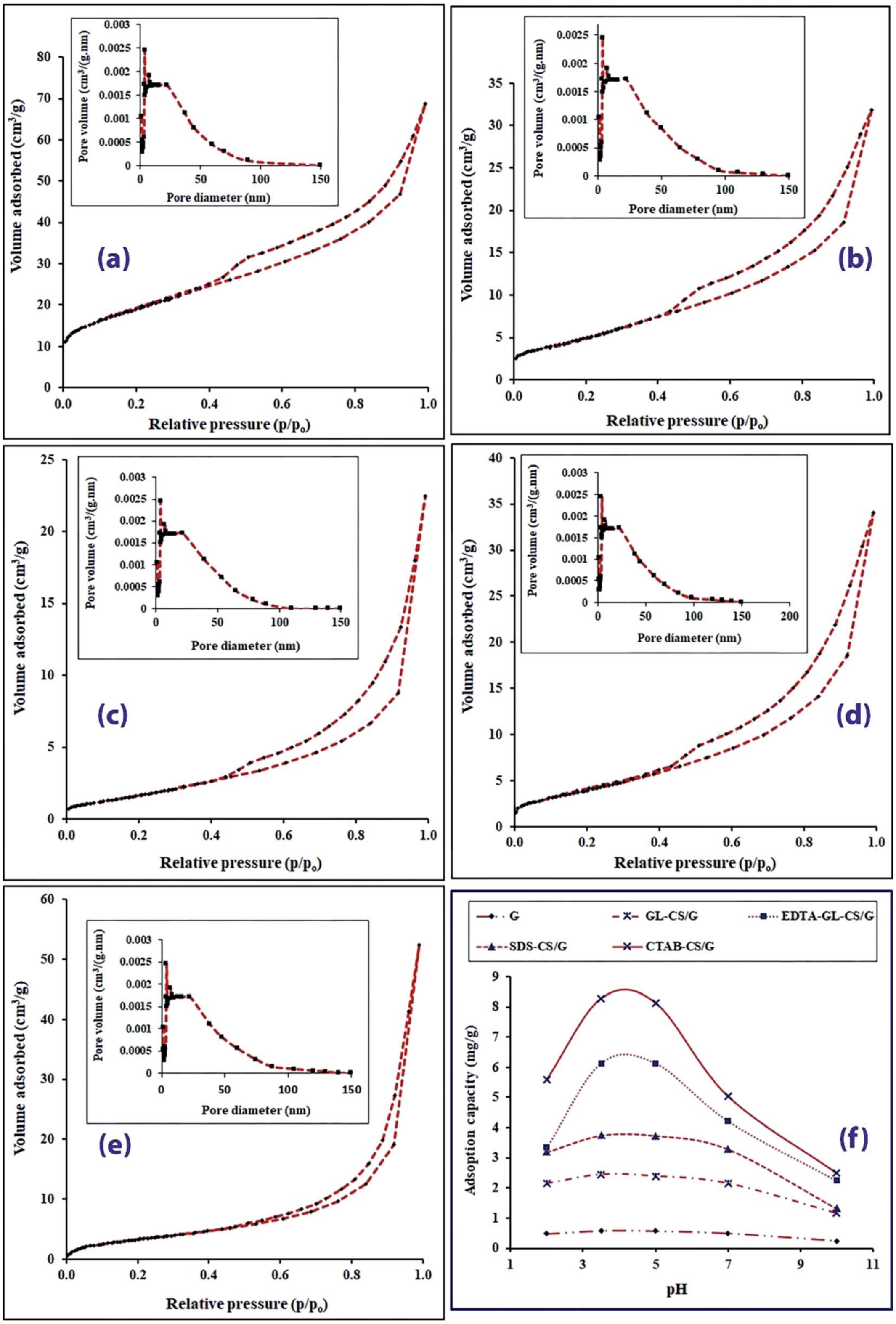

Fig. 4 N_2 adsorption–desorption isotherms of G (a), GL-CS/G (b), EDTA-GL-CS/G (c), SDS-CS/G (d), and CTAB-CS/G (e) products (the insets are the corresponding BJH pore-size distribution), and effect of pH on the F^- ion adsorption on the products (f).

determined by using nitrogen gas adsorption–desorption isotherm measurements for the products and the results are displayed in Fig. 4(a–e). It is clearly obvious that the as-prepared products showed type-IV isotherms with a hysteresis phenomenon of H3 type, as depicted in Fig. 4(a–e), according to the IUPAC classification.[46] These results imply the mesoporous nature of the G clay products. Interestingly, the BET surface area of the G, GL-CS/G, EDTA-GL-CS/G, SDS-CS/G, and CTAB-CS/G products were determined to be 67.16, 19.80, 15.80, 7.05, 12.78 $m^2 g^{-1}$, respectively. It can be easily concluded that coating process of the G clay and incorporation of the chitosan polymer and other organic species into its porous structures resulted in the noticeable reduction in the surface area of the G clay compared to the prepared composites. Similar trends have been reported before.[47] It is worth mentioning that the BET surface area of CTAB-CS/G is greater than that of SDS-CS/G composite, which is consistent with the obtained SEM results. The Barret–Joyner–Halenda (BJH) pore volume and pore diameter of the G, GL-CS/G, EDTA-GL-CS/G, SDS-CS/G, and CTAB-CS/G products were found to be (10.64 $cm^3 g^{-1}$; *ca.* 13.55 nm), (0.049 $cm^3 g^{-1}$; *ca.* 15.23 nm), (0.053 $cm^3 g^{-1}$; *ca.* 17.35 nm), (0.034 $cm^3 g^{-1}$; *ca.* 19.71 nm), and (0.081 $cm^3 g^{-1}$; *ca.* 22.38 nm), respectively. The Barrett–Joyner–Halenda (BJH) pore size distribution displayed in the insets of Fig. 4(a–e), indicated that the average pore diameter of as-prepared composites has high values compared to G and falls into the mesoporous category (less than 50 nm). The results also indicated that although the chitosan and organic species inserted into and coated some pores of the G clay, the total number of pores of the composites increased due to the high porosity of the modified chitosan polymer. This might facilitate the F^- anion removal through diffusion of these anions into these pores.

3.2. Adsorption studies

The adsorption characteristics of G, GL-CS/G, EDTA-GL-CS/G, SDS-CS/G, and CTAB-CS/G adsorbents were examined utilizing F^- ion as a pollutant model. Accordingly, different parameters controlling the adsorption process were tested such as media pH, adsorbent dosage, contact time, initial F^- ion concentration, and temperature.

3.2.1. Effect of pH. To examine the impact of pH on F^- ion adsorption, batch equilibrium investigations are conducted at different pH values in the range of 2–10. Fig. 4(f) displays the effect of initial pH on the performance of the F^- ion removal on G, GL-CS/G, EDTA-GL-CS/G, SDS-CS/G, and CTAB-CS/G adsorbents with 24 h stirring time. The adsorption working conditions were 50 mL of F^- ion solution with an initial concentration (C_0) of 50 mg L^{-1}, a specific mass of the adsorbent (2 g for G adsorbent or 0.1 g for GL-CS/G, EDTA-GL-CS/G, SDS-CS/G, and CTAB-CS/G adsorbents, respectively), and 25 °C temperature. The results revealed that the F^- ion adsorption first enhanced with increasing the pH until it attained the equilibrium at pH 3.5 and then declined with increasing the pH value. A similar trend has been published elsewhere.[48] The drops in F^- ion uptake with increasing pH were seemingly due to the change of adsorbents surface charge. At an acidic pH value of less than 2, F^- ion removal was low because very high acidity induced the generation of weak hydrofluoric acid which hindered the adsorption of F^- ion.[49] With a gradual increase in pH up to 3.5, the surface of adsorbent was highly protonated and the ionization of sodium fluoride increased, and hence the positively charged surface sites of the adsorbent have been evolved. With increasing the pH value above 3.5, these adsorption sites are gradually de-protonated causing hydroxide ions generation, which are adsorptive competitor to F^- ions resulting in a decline in the adsorption.

In case of using GL-CS/G, EDTA-GL-CS/G, SDS-CS/G, and CTAB-CS/G adsorbents at lower pH, parts of $-NH_2$ groups were protonated; consequently, raising electrostatic attraction between negatively charged F^- ion and positively charged adsorption sites of chitosan chains enhances the adsorption.[50] On the contrary, with increasing the pH value the amino groups are deprotonated and abundant OH^- ions generated a competitive situation with anionic F^- ion for the adsorption sites due to the electrostatic repulsion between the negatively charged surface sites of the adsorbent and F^- ion; thus the F^- ion removal declines. It must be noted that the relatively low F^- ion sorption efficiency on G clay compared with other modified forms is most likely caused by a high content of silicates which having a negative charge, electrostatically repel F^- ion, thus blocking its sorption. Similar findings have been stated earlier.[51] Therefore, all the following operations were performed at pH 3.5.

3.2.2. Effect of adsorbent dosage. The effect of adsorbent dosage on F^- ion was studied under the former working conditions except for the amount of adsorbent as depicted in Fig. 5(a and b). The results showed that the adsorption of F^- ion was enhanced as the quantity of adsorbent increased. This might be due to that at a fixed initial concentration of sorbate the rise in the adsorbent amount afforded more adsorptive sites.[52] This improvement in adsorption proceeded until a particular dose of adsorbent, and then remained constant or decreased. The decrease in the adsorption efficiency is probably due to that increasing the adsorbent dosage is sometimes resulting in particle aggregation. This aggregation brings about a drop in the total adsorbent surface area and consequently a decrease in the available adsorption active sites, resulting in reduction in the adsorption efficiency.[53] Based on the attained results, 2 g of G or 0.1 g of GL-CS/G, EDTA-GL-CS/G, SDS-CS/G, and CTAB-CS/G was selected as the optimum adsorbent dosage for subsequent studies. The results also revealed that the adsorption capacities enhanced in the order of CTAB-CS/G > EDTA-GL-CS/G > SDS-CS/G > GL-CS/G > G. This behavior might be interpreted based on the fact that the chitosan was intercalated in G clay throughout the preparation process of composites, which expanded the interlayer spacing. This expansion can improve the F^- ion adsorption. CTAB-CS/G composite has showed the highest adsorption capacity toward F^- ions compared with other adsorbents; this may be due to functionalization of the G clay with positively charged cationic surfactant. The presence of CTAB surfactant in the CTAB-CS/G composite may change the G surface from hydrophilic to hydrophobic which might have enhanced the F^- ion adsorption onto its external surface and into the interlayer spacing.

3.2.3. Effect of contact time. The effect of contact time on F^- ion adsorption was explored by varying the contact time between F^- ion adsorbate and the adsorbents of interest in the range of 0–300 min under operation conditions: 50 mL of F^- ion solution with an initial concentration of 50 mg L^{-1}, 25 °C temperature, 3.5 pH, and a specific mass of the adsorbent (2 g

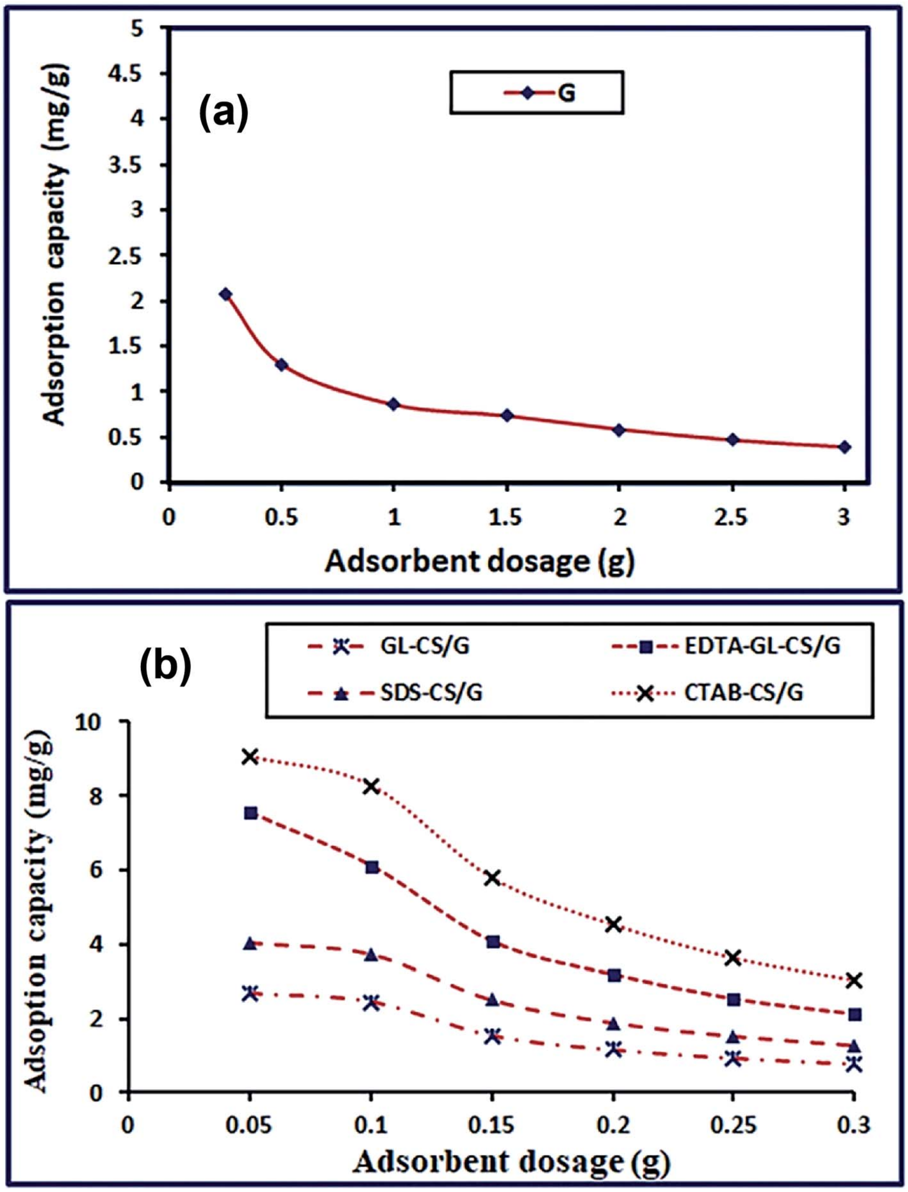

Fig. 5 Effect of adsorbent dosage on the F^- ions adsorption on G (a); GL-CS/G, EDTA-GL-CS/G, SDS-CS/G, and CTAB-CS/G (b) adsorbents.

for G adsorbent or 0.1 g for GL-CS/G, EDTA-GL-CS/G, SDS-CS/G, and CTAB-CS/G adsorbents, respectively). Fig. 6(a) demonstrated that the removal efficiency of F^- ion improved by extending the contact time. The rate of F^- ion uptake using G adsorbents was initially fast and then slowed down progressively until reached saturation after 120 min, which was fixed as their optimum contact time for further examinations. GL-CS/G, EDTA-GL-CS/G, SDS-CS/G, and CTAB-CS/G composites exhibited more powerful adsorption capacity and attained equilibrium after 180 min, which was fixed as their optimum contact time for further investigations. The rapid uptake throughout the initial stage of adsorption is seemingly due to the availability of substantial number of vacant active sites on the surface of adsorbents. However, the slower rates at more extended contact times are reasonably owing to slow pore diffusion of F^- ions into the adsorbent particles.[54]

3.3. Adsorption kinetics

To gain more knowledge into the adsorption mechanism and effectiveness of adsorption, some kinetic models have been considered such as pseudo-first-order, pseudo-second-order, and intra-particle diffusion models. The linear forms of pseudo-first-order (eqn (4)) and pseudo-second-order (eqn (5)) kinetic models are denoted as follows:[55–57]

$$\log(q_e - q_t) = \log q_e - (k_1/2.303)t \tag{4}$$

$$t/q_t = 1/(k_2 q_e^2) + (1/q_e)t \tag{5}$$

where, t (min) is the elapsed contact time, k_1 (min^{-1}) is the first-order rate constant, q_e (mg g^{-1}) is the adsorption capacity of the adsorbent for F^- ion at equilibrium, q_t (mg g^{-1}) is the adsorption capacity of the adsorbent for F^- ion at t time, and k_2 is the

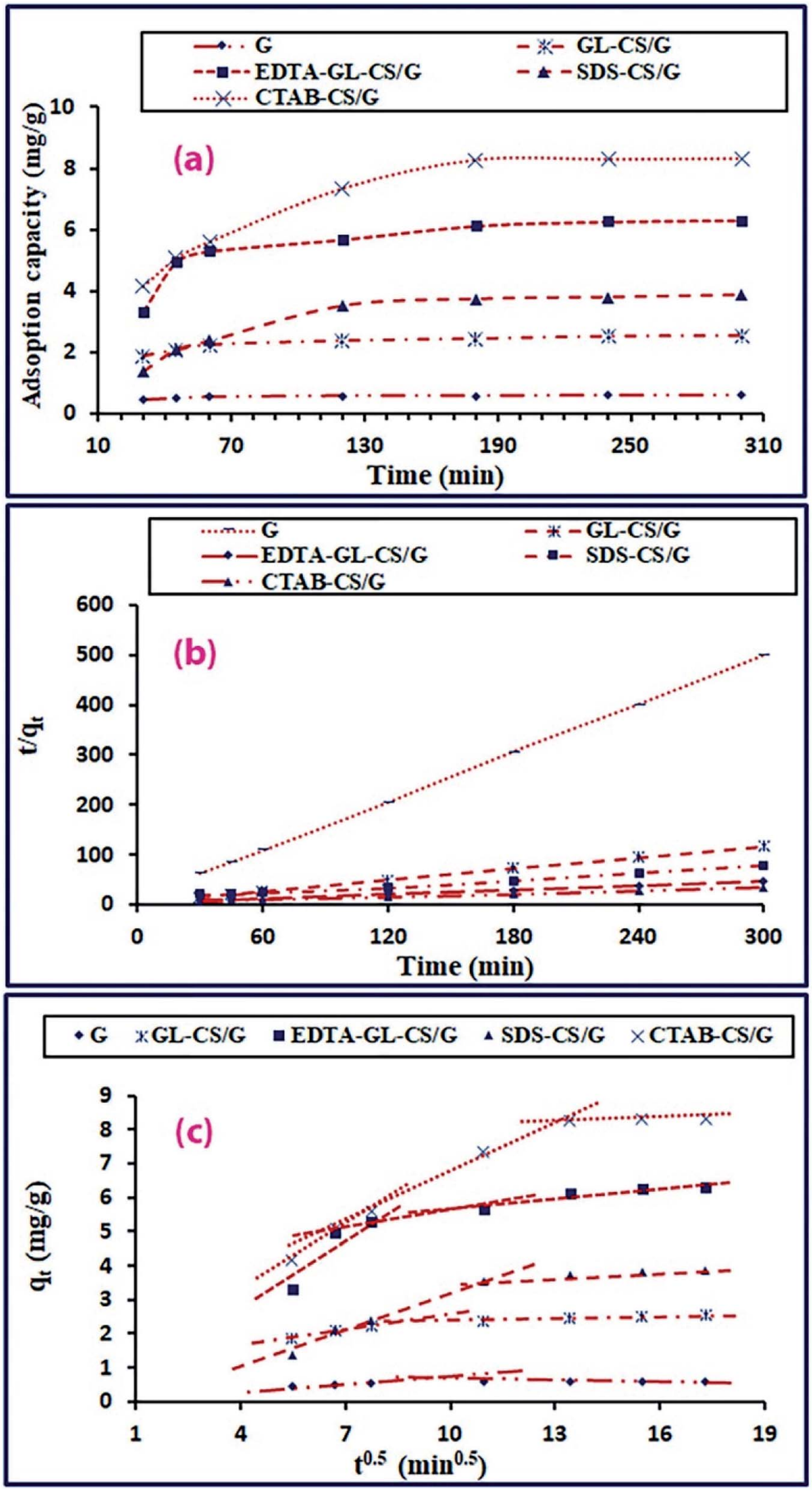

Fig. 6 Effect of contact time (a), and the pseudo-second-order kinetic model (b), and validation of intra-particle diffusion model (c) for F^- ions adsorption on G, GL-CS/G, EDTA-GL-CS/G, SDS-CS/G and CTAB-CS/G adsorbents.

second-order rate constant (g mg^{-1} min^{-1}). Values of k_1 and q_e constants of the pseudo-first-order kinetic model were determined from a plot of $\log(q_e - q_t)$ *versus* t (results not shown). The kinetic parameters—k_1 and correlation coefficients (R^2)—are listed in Table 2. From the values of the presented constants, it can be deduced that pseudo-first-order model does not apply

Table 2 Kinetic parameters for F^- ions adsorption on G, GL-CS/G, EDTA-GL-CS/G, SDS-CS/G, and CTAB-CS/G adsorbents

			Pseudo-first-order			Pseudo-second-order			Intra-particle diffusion		
Adsorbent	C_0 (mg L^{-1})	$q_{e(exp)}$ (mg g^{-1})	R^2	k_1 (1 min^{-1})	$q_{e(cal)}$ (mg g^{-1})	R^2	k_2 (g (mg min)$^{-1}$)	$q_{e(cal)}$ (mg g^{-1})	R^2	k_i (mg (g min$^{0.5}$)$^{-1}$)	C (mg g^{-1})
G	50	0.585	0.901	0.010	0.618	0.999	0.190	0.620	0.801	0.01	0.45
GL-CS/G	50	2.41	0.964	0.010	2.590	0.999	0.030	2.64	0.876	0.05	1.74
EDTA-GL-CS	50	6.13	0.904	0.007	6.656	0.998	0.006	6.823	0.747	0.21	3.22
SDS-CS/G	50	3.75	0.909	0.008	4.154	0.990	0.004	4.744	0.873	0.20	0.73
CTAB-CS/G	50	8.29	0.902	0.010	8.690	0.995	0.002	9.489	0.917	0.35	2.92

to the present adsorption study. On the other hand, values of k_2 and q_e constants of the pseudo-second-order model can be estimated by manipulating the slope and intercept of the plot t/q_t *versus* t (Fig. 6(b)). The parameters—k_2 and correlation coefficients (R^2)—of the pseudo-second-order model are presented in Table 2. The results manifested that the pseudo-second-order model described well the current adsorption process since the experimentally acquired $q_{e(exp)}$ values from this model are more in line with the estimated $q_{e(cal)}$ values. Furthermore, the R^2 values of this model are closer to 1.

Additionally, to understand the diffusion mechanism of the F^- ion adsorption, Weber's intra-particle diffusion model (eqn (6)) was applied to define the rate-controlling step of the present adsorption process.[58]

$$q_t = k_{id}t^{0.5} + c \quad (6)$$

where k_{id} (mg g^{-1}) min$^{-1/2}$ is the intra-particle diffusion rate constant and C (mg g^{-1}) is the intercept. The more substantial the value of intercept, the more prominent is the contribution of the surface adsorption in the rate-controlling step. In this model, q_t values were graphed against $t^{0.5}$. If the intra-particle diffusion is the only rate-limiting step, the plot should give a straight line reaching the origin. However, in the current study, plots of q_t *versus* $t^{1/2}$ (Fig. 6(c)) did not cross the origin and they were multilinear. Notably, the discrepancy between the mass transfer rate from the bulk liquid to the external surface of the particles for the initial and final stages of adsorption resulted in a divergence of the straight lines from the origin.[54] Moreover, the attained results designated that the adsorption of F^- ions on the G clay and its composites was controlled by different mechanisms like bulk diffusion, intra-particle diffusion, and film diffusion, and not only by the intra-particle diffusion mechanism.[54]

3.4. Adsorption isotherm studies

To examine the adsorption mechanism as well as the interaction between the adsorbate and the adsorbent at equilibrium, the adsorption data were tested using some isotherm models such as Langmuir, Freundlich, and Dubinin–Radushkevich models. Langmuir isotherm suggests a monolayer, homogenous adsorption and the adsorbed molecules do not have any interactions between each other. Freundlich isotherm designates a multilayer adsorption of the adsorbate species on heterogeneous surfaces. The linearized models of Langmuir and Freundlich isotherm equations can be arranged as in eqn (7) and (8), respectively.[59,60]

$$C_e/q_e = 1/(bq_m) + C_e/q_m \quad (7)$$

$$\ln q_e = \ln K_F + (1/n)\ln C_e \quad (8)$$

where C_e is the equilibrium F^- ion concentration (mg L^{-1}), q_e is the quantity of F^- ion adsorbed per unit weight of adsorbent (mg g^{-1}), q_m is the maximum adsorption capacity (mg g^{-1}), and b is Langmuir constant (L mg^{-1}). Furthermore, K_F [(mg g^{-1})(L mg^{-1})$^{1/n}$] and n are Freundlich constants which indicate adsorption capacity and adsorption intensity of the F^- ions on the adsorbents of interest, respectively.

Based on the Langmuir adsorption isotherm, q_m and b values were computed from the linear regression analysis of the plot of C_e/q_e *vs.* C_e as displayed in Fig. 7(a). Moreover, according to the Freundlich adsorption isotherm, the Freundlich constants (n and K_F) are computed using the plot of ln q_e *vs.* ln C_e through its intercept and slope (Fig. 7(b)). The Langmuir and Freundlich isotherm constants are tabulated in Table 3. Furthermore, eqn (9) is utilized to calculate the maximum adsorption capacity (q_m), according to the Freundlich isotherm model.[61]

$$K_F = q_m/C_0^{(1/n)} \quad (9)$$

According to the listed data in Table 3, the Langmuir isotherm model agreed well to the experimental data, compared to the Freundlich isotherm model. This is attributing to the following: the Langmuir model has higher R^2 values and maximum adsorption capacities; and q_m ($q_{m(cal)}$), gained from this model is agreeing with the experimental q_m ($q_{m(exp)}$). The validity of the Langmuir isotherm model implies the homogeneous nature of adsorbents of interest and the monolayer coverage of the adsorption of F^- ions on those adsorbents. Moreover, according to the Langmuir isotherm model, the q_{max} values are found to be in the order of CTAB-CS/G > EDTA-GL-CS/G > SDS-CS/G > GL-CS/G > G. High adsorption efficiency of CTAB-CS/G adsorbent can be explained as the presence of negative surface charge of the G clay with a large amount of exchangeable positive ions can result in covering its surface with a layer of water molecule; therefore, it exhibits strong

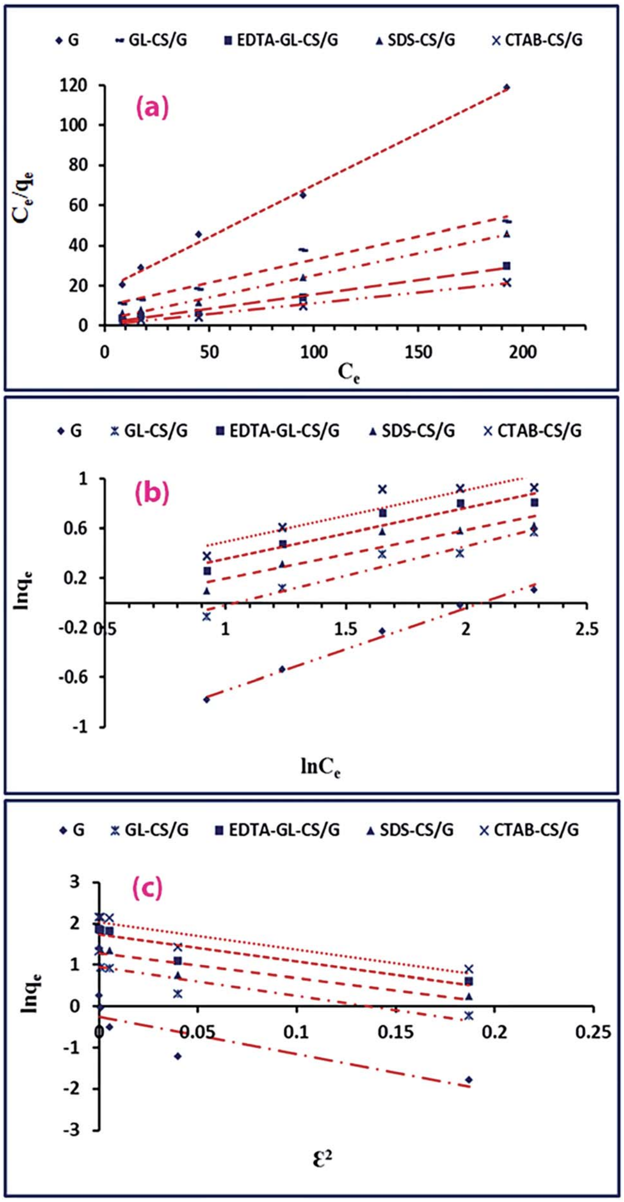

Fig. 7 Langmuir isotherm (a), Freundlich isotherm (b), and Dubinin–Radushkevich isotherm (c) models for the F^- ions adsorption on G, GL-CS/G, EDTA-GL-CS/G, SDS-CS/G and CTAB-CS/G adsorbents.

hydrophilicity and relatively low adsorption capacity towards F^- ions. However, complexation with chitosan polymer containing large numbers of –OH and –NH_2 functional groups can enhance their adsorption capacity towards F^- ions. As a consequence of functionalization by organic cations such as cationic surfactants (CTAB), the surface properties can be changed from hydrophilic to hydrophobic, thus more enhancement in their adsorption capacity towards F^- ions is obtained. CTAB molecule has a polar positively charged head group ($N^+(CH_3)_3$), which makes positive surface potential when it is pointed towards the bulk of the solution. Consequently, strong electrostatic interaction between positive charged CTAB head and F^- ions would be enhanced. Another probable mechanism is the electrostatic attraction between surfactant cations and negatively charged groups of CS molecules because –OH groups of CS molecules lose hydrogen ions in alkali coagulating solution. In both mechanisms, surfaces of CTAB-CS/G beads receive a confident potential, which increases the removal of F^- ions. Moreover, G surfaces have both negative and positive functional groups to attract free ions in aqueous solution.

In addition, the adsorption effectiveness of F^- ions on the adsorbents under research can be presented by the separation factor constant (R_L) as follows:

$$R_L = 1/(1 + bC_0) \qquad (10)$$

where C_0 (mg L^{-1}) and b (L mg^{-1}) have the previously designated meaning. According to the R_L values: $R_L = R_L > 1$, $R_L = 1$, 0, or $0 < R_L < 1$; it can be established whether the isotherm type of the adsorption is unfavorable, linear, irreversible, or favorable, respectively.[62] The separation parameter (R_L) values for the adsorption process were evaluated at initial concentrations from 10 to 200 mg L^{-1} and presented in Table 4; the R_L values were observed to be lying between 0 and 1, which symbolized favorable adsorption of F^- ion on G, EDTA-GL-CS/G, SDS-CS/G, and CTAB-CS/G surfaces at all F^- ion concentrations. Besides, the adsorption of F^- ions is favorable because the calculated Freundlich exponent (n) values are in the range of 1.84–2.76.[63]

To understand the nature of the adsorption, the equilibrium data were analyzed by applying the Dubinin–Radushkevich isotherm model (D–R model). The linearized form of the D–R model can be displayed as provided in eqn (11).[64]

$$\ln q_e = \ln q_m - \beta\varepsilon^2 \qquad (11)$$

where ε (Polanyi potential) = $RT\ln(1 + (1/C_e))$, q_e (mg g^{-1}) is the adsorption capacity of the adsorbent at equilibrium, q_m (mg g^{-1}) is the maximum adsorption capacity, β(mol^2 kJ^{-2}) is the Dubinin–Radushkevich constant correlated to the adsorption energy, R(8.314 J $(mol\ K)^{-1}$) is the universal gas constant and T (K) is the absolute temperature. q_m and β values can be estimated from the plot of ln q_e against ε^2 by utilizing its the slope and intercept, as depicted in Fig. 7(c). The correlation coefficients in the D–R model were ascertained to be lower than those of Freundlich and Langmuir isotherm models, as manifested in Table 3. The mean free energy of adsorption (E), designated as the free energy change when 1 mol of ions is transported to the surface of the solid from infinity in a solution, can be computed from the next equation (eqn (12)).

$$E = \sqrt{(1/2\beta)} \qquad (12)$$

The quantity of E is beneficial for reasoning the type of adsorption and if the value is within 8 and 16 kJ mol^{-1}, the adsorption type can be described by ion exchange. For E values <8 kJ mol^{-1}, the adsorption process is a physical adsorption.[65] The current study revealed that the calculated E values were <8 kJ mol^{-1}, indicating the physisorption of F^- ions on the adsorbents under research. Nevertheless, the D–R model did not apply well to the experimental adsorption data as it gave lower R^2 values and the estimated q_m values were not

Table 3 Isothermal parameters for F^- ions adsorption on G, GL-CS/G, EDTA-GL-CS/G, SDS-CS/G, and CTAB-CS/G adsorbents

		Langmuir isotherm parameters			Freundlich isotherm parameters				D–R isotherm parameters			
Adsorbent	$q_{m(exp)}$ (mg g^{-1})	$q_{m(cal)}$ (mg g^{-1})	b (L mg^{-1})	R^2	$q_{m(cal)}$ (mg g^{-1}) (for $C_0 = 10–200$ mg L^{-1})	K_F ((mg g^{-1}) (L $mg^{-1})^{1/n}$)	n	R^2	q_m (mg g^{-1})	β (mg $g^{-1})^2$	E (kJ mol^{-1})	R^2
G	1.26	1.15	0.028	0.991	0.320–1.62	0.0910	1.84	0.989	0.750	3.550	0.370	0.727
GL-CS/G	3.75	4.31	0.023	0.961	0.960–3.98	0.319	2.10	0.945	2.63	16.97	0.178	0.824
EDTA-GL-CS/G	6.32	6.90	0.074	0.993	2.59–8.15	1.07	2.61	0.835	5.73	9.450	0.232	0.859
SDS-CS/G	4.17	4.55	0.060	0.996	1.65–5.04	0.698	2.68	0.868	3.68	11.97	0.204	0.892
CTAB-CS/G	8.45	9.03	0.096	0.995	3.71–11.0	1.61	2.76	0.822	7.68	6.600	0.275	0.869

Table 4 Dimensionless separation factor (R_L) calculated from Langmuir constant (b) for F^- ion adsorption on G, GL-CS/G, EDTA-GL-CS/G, SDS-CS/G, and CTAB-CS/G adsorbents

Initial F^- ion concentration (mg L^{-1})	G	GL-CS/G	EDTA-GL-CS/G	SDS-CS/G	CTAB-CS/G
10	0.781	0.813	0.574	0.625	0.510
20	0.641	0.179	0.403	0.454	0.342
50	0.416	0.465	0.212	0.250	0.208
100	0.263	0.303	0.119	0.143	0.094
200	0.151	0.178	0.063	0.076	0.049

comparable to the $q_{m(exp)}$ values. Consequently, the Langmuir isotherm model could well explain the practically obtained adsorption data, comparing to the other examined isothermal models.

3.5. Thermodynamic study

The impact of temperature on the adsorption of F^- ions on the adsorbents of concern was studied at varying temperatures (298–318 K). The results showed that the temperature has a notable influence on the adsorption of F^- ions, and the performance of F^- ions adsorption on G, GL-CS/G, EDTA-GL-CS/G, SDS-CS/G, and CTAB-CS/G adsorbents was different. The removal efficiency of F^- ions declined for the worked adsorbents on raising the temperatures.

In addition, thermodynamic parameters associated with the adsorption: Gibbs free energy change (ΔG^0), entropy change (ΔS^0), and enthalpy change (ΔH^0), have been evaluated by applying eqn (13) and (14).[66,67]

$$\ln K_c = \Delta S^0/R - \Delta H^0/RT \quad (13)$$

$$\Delta G^0 = \Delta H^0 - T\Delta S^0 \quad (14)$$

where T and R are absolute temperature (K) and universal gas constant (8.314 J mol^{-1} K^{-1}), respectively. According to eqn (15), K_c is a thermodynamic equilibrium constant with a dimensionless unit. In this light, some proposals were recommended to ensure the thermodynamic equilibrium constant is dimensionless.[67–69]

$$\Delta G^0 = -RT \ln K_c \quad (15)$$

In the current research, the dimensionless thermodynamic equilibrium constant (K_c) was assessed by applying the distribution coefficient constant (K_d) strategy.[68] In this respect, the distribution coefficient constant ($K_d = q_e/C_e$) was first assessed by graphing $\ln(q_e/C_e)$ against q_e and extrapolating q_e to zero. Then K_d was corrected according to the approach introduced by Milonjić to get the thermodynamic equilibrium constant K_c ($K_c = K_d \times 1000$).[69] Based on eqn (13), plotting $\ln K_c$ against $1/T$ (Fig. 8(a)) can be exploited to evaluate ΔH^0 and ΔS^0 values. The ΔG^0 values can be assessed by supplying the evaluated ΔH^0 and ΔS^0 values into eqn (14). The thermodynamic constants are compiled in Table 5. The results revealed that ΔG^0 values were in the ranges (from −7.66 to −8.05), (from −11.9 to −12.1), (from −15.4 to −16.1), (from −12.8 to −13.4), and (from −14.3 to −15.1 kJ mol^{-1}) for G, GL-CS/G, EDTA-GL-CS/G, SDS-CS/G, and CTAB-CS/G adsorbents, respectively. The obtained results indicate the spontaneity nature of the adsorption of F^- ions. In addition, the adsorption of F^- ions on the aforementioned adsorbents is a physisorption process since ΔG^0 values are in the range of (−20) to (0) kJ mol^{-1}. The adsorption of F^- ions on the adsorbents under examination is exothermic, attributing to the gained ΔH^0 negatives values. The values of the evaluated ΔH^0 are less than 40 kJ mol^{-1}, which proposing the physisorption nature of the adsorption of F^- ions on the adsorbents of interest. The positive ΔS^0 for all adsorbents referred the increase in the randomness at the solid-solution interface throughout the adsorption process.

3.6. Comparison with different adsorbents

Table 6 outlines the comparison of the maximum adsorption capacities of numerous adsorbents for F^- ion. The results

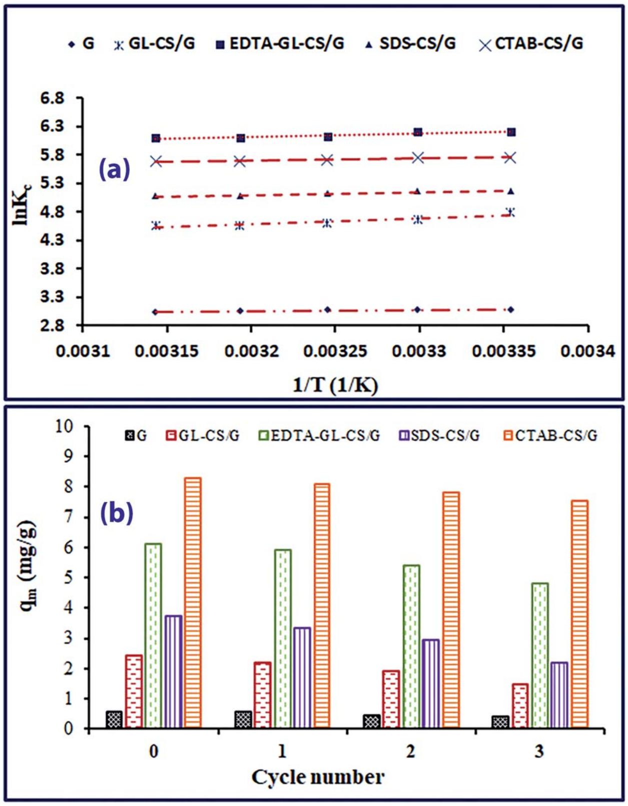

Fig. 8 Plots of ln K_C *versus* $1/T$ for F^- ions adsorption on G, GL-CS/G, EDTA-GL-CS/G, SDS-CS/G and CTAB-CS/G adsorbents (a) and regeneration efficiency of the adsorbents (b).

Table 6 Fluoride ion adsorption capacity of various adsorbents

Adsorbent	F^- q_{max} (mg g^{-1})	Reference
Modified kaolinite clay	0.1	75
La(III)-loaded bentonite/chitosan beads (La-BCB)	2.87	76
Glauconite (G)	1.152	This study
Montmorillonite clay	1.49	77
Montmorillonite chitosan biocomposite (MMT@CS)	1.83	78
Modified chitosan-glauconite composite (GL-CS/G)	4.31	This study
SDS-modified glauconite (SDS-CS/G)	4.55	This study
EDTA-modified glauconite (EDTA-GL-CS/G)	6.90	This study
CTAB-modified glauconite (CTAB-CS/G)	9.03	This study
Modified attapulgite	11.1	79

demonstrated that G, GL-CS/G, EDTA-GL-CS/G, SDS-CS/G, and CTAB-CS/G adsorbents are superior to several other adsorbents for F^- ion adsorption, reflecting a promising utility for these adsorbents in F^- ion removal from contaminated water. Although the adsorption capacity of G was lower when correlated to that of its adjusted forms, it was found to be satisfactory with the most common adsorbents. Variations in adsorption capacities between several adsorbents are arising from variation in chemical and structural properties, the surface of the adsorbents as well as from the applied practical conditions. Chen *et al.*[70] have demonstrated that the F^- ion adsorption capacity of clay adsorbents is correlated to aluminum and iron contents of the adsorbent. Therefore, it can be inferred that the high fluoride adsorption capacity of G and its composites is seemingly due in part to the high Fe content in G clay, high porosity of the composites, and functionalization with head-groups of the SDS and CTAB surfactants.

3.7. Regeneration studies

Effective reuse of adsorbent material affects the expense factor and hence its efficiency in many cycles of operation. The efficiency of G, GL-CS/G, EDTA-GL-CS/G, SDS-CS/G, and CTAB-CS/G adsorbents for the removal of F^- ion was examined by studying the recovery and reusability of the as-synthesized gluconite adsorbents. This was accomplished by conducting the adsorption of F^- ion, under the optimal conditions utilizing 50 mg L^{-1} F^- ion concentration, 3 h contact time, and pH 3.5 at room temperature (*ca.* 25 °C ± 1) and reproduced for three cycles. The applied adsorbents were recovered in 0.5 M NaOH and washed with deionized water accompanied by drying in oven at 50 °C, and the gathered data were manifested in Fig. 8(b). The maximum adsorption capacities (q_m) for each sorption/desorption cycle were determined to be 0.578, 0.470, and 0.400 mg g^{-1} for G; 2.20, 1.91, and 1.5 mg g^{-1} for GL-CS/G; 5.91,

Table 5 Thermodynamic parameters for F^- ions adsorption on G, GL-CS/G, EDTA-GL-CS/G, SDS-CS/G and CTAB-CS/G adsorbents

	T (K)											
	K_c at different K temperatures					ΔG^0 (kJ mol^{-1}) at different K temperatures						
Adsorbent	298	303	308	313	318	298	303	308	313	318	ΔH^0 (kJ mol^{-1})	ΔS^0 (kJ $(mol\ k)^{-1}$)
G	21.99	21.85	21.86	21.22	21.02	−7.66	−7.77	−7.90	−7.95	−8.05	−1.86	0.019
GL-CS/G	120.3	106.5	100.9	96.66	95.95	−11.9	−11.8	−11.8	−11.9	−12.1	−8.74	0.013
EDTA-GL-CS/G	504.8	498.8	454.2	452.7	446.9	−15.4	−15.7	−15.7	−15.9	−16.1	−5.38	0.033
SDS-CS/G	176.0	175.7	168.8	161.4	160.3	−12.8	−13.0	−13.1	−13.2	−13.4	−4.28	0.028
CTAB-CS/G	318.1	315.4	304.9	295.9	298.7	−14.3	−14.5	−14.6	−14.8	−15.1	−2.99	0.037

5.40, and 4.82 mg g^{-1} for EDTA-GL-CS/G; 3.33, 2.93, and 2.20 mg g^{-1} for SDS-CS/G; as well as 8.11, 7.82, and 7.53 mg g^{-1} for CTAB-CS/G. These results exhibited that the adsorbents have a remarkable regeneration capability and reliable performance for duplicated performance up to at least 3 cycles. Therefore, the gained results and the facile synthesis route imply that the modified G clay structures are promising and relevant nominees for the elimination of F^- ions from aqueous solutions. The results also refer to a long-term application of the adjusted clay structures for the adsorptive elimination of F^- ion from aqueous media.

3.8. Mechanism of F^- ions adsorption on G clay and its modified forms

This study revealed that the pH factor has an essential role in the adsorption of F^- ions on the G clay and the as-prepared composites. The highest adsorption efficiency occurred at acidic pH values (pH 3.5) and this efficiency decreased at higher pH values. It is clearly seen that the mechanism of the adsorption depends also on the structure of the applied adsorbent. Accordingly, the proposed fluoride adsorption mechanism is outlined in Scheme 1. The glauconite (G) clay contains various hydrous oxides especially those of silicate, iron, and aluminum. The adsorption of the contaminants frequently takes place at surface hydroxylated sites of the clay, which are represented as GOH, in Scheme 1. These hydroxo groups are amphoteric; hence they undergo protonation in the acidic media and converted into positive surface hydroxylated sites (GOH_2^+), according to eqn (1) in Scheme 1. The adsorption of F^- ions can mainly be explained by the following two mechanisms. These probable mechanisms are a two-step anion exchange mechanism (eqn (1) and (2); Scheme 1) and electrostatic attraction mechanism between the oppositely charged F^- ions and the protonated hydroxylated sites (eqn (3); Scheme 1). These findings are consistent with some reported mechanisms for adsorptive removal of some anions.[70] Furthermore, for chitosan composites (GL-CS/G, EDTA-GL-CS/G, SDS-CS/G, and CTAB-CS/G), the chitosan $-NH_2$ groups are protonated at lower

$$\mathrm{GOH} + \mathrm{H^+} \longrightarrow \mathrm{GOH_2^+} \tag{1}$$

$$\mathrm{GOH_2^+} + \mathrm{F^-} \longrightarrow \mathrm{GF} + \mathrm{H_2O} \tag{2}$$

$$\mathrm{GOH_2^+} + \mathrm{F^-} \longrightarrow \mathrm{GOH_2^+}\cdots\cdots\mathrm{F^-} \tag{3}$$

$$\mathrm{R^1NH_2} + \mathrm{H^+} \longrightarrow \mathrm{R^1NH_3^+} \tag{4}$$

$$\mathrm{R^1NH_3^+} + \mathrm{F^-} \longrightarrow \mathrm{R^1NH_3^+}\cdots\cdots\mathrm{F^-} \tag{5}$$

$$\mathrm{R^2COO^-} + \mathrm{H^+} \longrightarrow \mathrm{R^2COOH} \tag{6}$$

$$\mathrm{R^2COOH} + \mathrm{F^-} \longrightarrow \mathrm{R^2COOH}\cdots\cdots\mathrm{F^-} \tag{7}$$

$$\mathrm{R^3{}_3N} + \mathrm{H+} \longrightarrow \mathrm{R^3{}_3NH+} \tag{8}$$

$$\mathrm{R^3{}_3NH^+} + \mathrm{F^-} \longrightarrow \mathrm{R^3{}_3NH^+}\cdots\cdots\mathrm{F^-} \tag{9}$$

$$\mathrm{R^4OSO_3^-} + \mathrm{H^+} \longrightarrow \mathrm{R^4OSO_3H} \tag{10}$$

$$\mathrm{R^4OSO_3H} + \mathrm{F^-} \longrightarrow \mathrm{R^4OSO_3H}\cdots\cdots\mathrm{F^-} \tag{11}$$

$$\mathrm{R^5N(CH_3)_3Br} + \mathrm{F^-} \longrightarrow \mathrm{R^5N(CH_3)_3F} + \mathrm{Br^-} \tag{12}$$

$$\mathrm{R^5N(CH_3)_3^+} + \mathrm{F^-} \longrightarrow \mathrm{R^5N(CH_3)_3^+}\cdots\cdots\mathrm{F^-} \tag{13}$$

Scheme 1 Proposed mechanism of the adsorption of F^- ions adsorption on G, GL-CS/G, EDTA-GL-CS/G, SDS-CS/G and CTAB-CS/G adsorbents. Where R^1, R^2, R^3, R^4, and R^5 are different aliphatic groups.

Table 7 Physico-chemical parameters of de-fluorinated real wastewater sample after its treatment using the as-prepared adsorbents

Water quality parameters	Content ($mg\ L^{-1}$) Before treatment	After treatment (the obtained range for applying G clay and its composites)
pH	3.12	3.50–3.65
Electrical conductivity ($\mu m\ cm^{-1}$)	9060	53.41–55.22
Turbidity (NTU)	51.00	70.00–78.00%
Total hardness ($mg\ L^{-1}$)	3100	37.00–40.00%
COD	180	71.00–73.00%
P ($mg\ L^{-1}$)	1800	37.00–39.10%
T.S ($mg\ L^{-1}$)	16 500	42.75–45.18%
T.D.S ($mg\ L^{-1}$)	13 300	40.00–43.84%
T.S.S ($mg\ L^{-1}$)	3200	61.41–64.23%
F ($mg\ L^{-1}$)	11.00	40.16–63.59%
CL ($mg\ L^{-1}$)	369.2	54.33–55.17%
Fe ($mg\ L^{-1}$)	518	10.00–17.00%
Na ($mg\ L^{-1}$)	610	60.00–70.00%
K ($mg\ L^{-1}$)	150	52.00–53.80%
S ($mg\ L^{-1}$)	3500	48.88–51.11%
Mg ($mg\ L^{-1}$)	190.10	67.11–70.10%
Mn ($mg\ L^{-1}$)	18.06	73.34–97.00%

pH values and hence the electrostatic attraction between the positively charged chitosan surface ($-NH_3^+$) and F^- anions are significant as well, as presented in eqn (4) and (5) in Scheme 1. Similar results have been reported for other chitosan composites.[71] The function groups of the EDTA in EDTA-GL-CS/G composite may also play a role in adsorption for this composite, according eqn (6) through (9) in Scheme 1. At lower pH values the carboxylate groups ($-COO^-$) of the EDTA can be protonated ($-COOH$) then in the presence of F^- anions a weak hydrogen bonding is probably formed between these anions and hydrogens of the protonated carboxylate groups. Besides, at $pH \leq 3.5$, the tertiary amino groups (R_3^3N) can also be protonated forming the positively charged ($R_3^3NH^+$) groups. The adsorption can also take place through electrostatic attractions between these positively charged amino groups ($R_3^3NH^+$) of the EDTA molecules and the existing F^- anions. This proposed adsorption mechanism is in good agreement with the reported one for similar molecules for EDTA.[72] For SDS-CS/G composite, the sulfonate headgroup of the SDS surfactant may also has a role in the adsorption process for this composite, as outlined in eqn (10) and (11) in Scheme 1. In which, the sulfonate groups ($-OSO_3^-$) may undergo protonation at acidic pH values. The adsorption may also be taken place through weak hydrogen bonding between the hydrogen atoms of the protonated sulfonate groups ($-OSO_3H$) and the F^- anions. Similar behavior has been reported for adsorption of some anionic dyes.[73] On the other hand, the CTAB-CS/G composite has more adsorptive active sites. In addition to the aforementioned adsorption mechanisms due to G clay and chitosan presence, the adsorption in this composite may also proceed through two additional mechanisms: (1) anion exchange between Br^- ions of the CTAB component and F^- anion of the solution (eqn (12); Scheme 1), and (2) electrostatic attraction between the positively charged headgroups ($R^5N(CH_3)_3^+$) of the CTAB components of the composite and the negatively charged F^- ions in the solution (eqn (13); Scheme 1). The proposed mechanism for CTAB-modified composite is compatible with those reported for similar cationic surfactants.[74] It is noticeable that the CTAB-CS/G composite has more active sites, particularly positively charged sites, for the adsorption process, which can explain its high efficiency compared to the other studied adsorbents. However, the G clay and the modified composites showed low adsorption efficiencies toward F^- removal at higher pH values. This is probably returning to the repulsive interactions between similar charged species—F^- anions and the negatively charged particles of the products.

3.9. Application to real water samples

The practical utilization of an adsorbent to real samples is the principal purpose of the adsorption process. The effectiveness of the examined adsorbent to real samples significantly implies its performance within reasonable wastewater handling methods. To explore the applicability of the analyzed adsorbents for F^- ion removal, the water samples were assembled from wastewater ponds before treatment in the treatment unit in Abu-Zaabal for Fertilizers and Chemicals Company (AZFC), Egypt. These ponds involve extensive land regions and adopted for assembling wastewater streams provided from different manufacturing processes of phosphatic fertilizers. Ten specimens of wastewater from various spots along the ponds are taken then homogenized and maintained at refrigerator at 4 °C for additional use. The chemical composition of wastewater was analyzed and compiled in Table 7. The batch adsorption experiments as reported in the Materials and methods section were conducted. The concentration of F^- ion in the filtrate was examined after applying preceding adsorbents. Interestingly, it is noticed that the maximum F^- ion removal reflected the trend of CTAB-CS/G > EDTA-GL-CS/G > GL-CS/G > G = SDS-CS/G with removal percent of 63.59%, 60.18%, 47.11%, 40.21% and 40.16%, respectively. Furthermore, the third-cycle-regenerated nanocomposites: CTAB-CS/G, EDTA-GL-CS/G, GL-CS/G, SDS-CS/G, and G, were applied to real water samples, and they exhibited significant removal percentages: 60.56%, 52.50%, 40.22%, 32.40%, and 31.10%, respectively. Indicating a high chemical stability and efficiency of the products for removing the F^- ion from wastewater although the wastewater samples contain various types of ions (cations and anions), which can well compete and interfere with the adsorption process.

4 Conclusions

In conclusion, various natural green sand (glauconite clay)/modified chitosan (CS) nanocomposites were successfully prepared by applying a facile mixing and a crosslinking combination method. In this light, ethylenediaminetetraacetic acid (EDTA), glutaraldehyde (GL), sodium dodecyl sulfate (SDS), and cetyltrimethyl ammonium bromide (CTAB) were selected for the chitosan modification. The as-prepared composites were identified using several means and implemented for the adsorptive elimination of fluoride ions from aqueous media utilizing a batch technique. The adsorbents showed good adsorption capacity in the subsequent order: raw glauconite (G) < GL-CS/G < SDS-CS/G < EDTA-GL-CS/G < CTAB-CS/G. The obtained maximum adsorption capacity values were 1.15, 4.31, 4.55, 6.90, and 9.03 mg g^{-1} for the adsorbents: glauconite (G), GL-CS/G, SDS-CS/G, EDTA-GL-CS/G, and CTAB-CS/G, respectively. The highest adsorption capacity of CTAB-CS/G composite may be owing to the contribution of its various function groups. Furthermore, different mechanisms have been proposed for the adsorptive removal of F^{-} ion using the adsorbents under investigation. The results revealed that the adsorption process followed the pseudo-second-order kinetic and Langmuir isotherm models and it was spontaneous and physisorption process. Besides, it can conclude that the modified chitosan adsorbents are hopeful candidates for the adsorptive removal of F^{-} ions from aqueous solutions based on its reusability, high endurance, good adsorption capacity, and appropriateness for actual field water samples.

Conflicts of interest

There are no conflicts to declare.

References

1 Organization WH, *Guidelines for drinking-water quality: World Health Organization*, Distribution and Sales, Geneva, 2011, vol. 27.

2 S. I. Alhassan, L. Huang, Y. He, L. Yan, B. Wu and H. Wang, Fluoride removal from water using alumina and aluminum-based composites: a comprehensive review of progress, *Crit. Rev. Environ. Sci. Technol.*, 2020, 1–35.

3 S. Vasudevan, J. Lakshmi and G. Sozhan, Studies on a Mg–Al–Zn Alloy as an Anode for the Removal of Fluoride from Drinking Water in an Electrocoagulation Process, *Clean: Soil, Air, Water*, 2009, **37**(4–5), 372–378.

4 E. J. Reardon and Y. Wang, A limestone reactor for fluoride removal from wastewaters, *Environ. Sci. Technol.*, 2000, **34**(15), 3247–3253.

5 C. Hu, S. Lo and W. Kuan, Effects of the molar ratio of hydroxide and fluoride to Al (III) on fluoride removal by coagulation and electrocoagulation, *J. Colloid Interface Sci.*, 2005, **283**(2), 472–476.

6 L. Anjaneyulu, E. A. Kumar, R. Sankannavar and K. K. Rao, Defluoridation of drinking water and rainwater harvesting using a solar still, *Ind. Eng. Chem. Res.*, 2012, **51**(23), 8040–8048.

7 G. Alagumuthu, V. Veeraputhiran and R. Venkataraman, Adsorption isotherms on fluoride removal: batch techniques, *Arch. Appl. Sci. Res.*, 2010, **2**(4), 170–185.

8 M. Y. Nassar, I. S. Ahmed and H. S. Hendy, A facile one-pot hydrothermal synthesis of hematite (α-Fe$_2$O$_3$) nanostructures and cephalexin antibiotic sorptive removal from polluted aqueous media, *J. Mol. Liq.*, 2018, **271**, 844–856.

9 M. Y. Nassar, E. I. Ali and E. S. Zakaria, Tunable auto-combustion preparation of TiO$_2$ nanostructures as efficient adsorbents for the removal of an anionic textile dye, *RSC Adv.*, 2017, **7**(13), 8034–8050.

10 S. Chidambaram, A. Ramanathan and S. Vasudevan, Fluoride removal studies in water using natural materials, *Water SA*, 2003, **29**(3), 339–344.

11 K. Gopal, S. Srivastava, S. Shukla and J. Bersillon, Contaminants in drinking water and its mitigation using suitable adsorbents: an overview, *J. Environ. Biol.*, 2004, **25**(4), 469–475.

12 S. Mayadevi, Adsorbents for the removal of fluoride from water, *Indian Chem. Eng., Sect. A*, 1996, **38**, 155–157.

13 B. Doušová, T. Grygar, A. Martaus, L. Fuitová, D. Koloušek and V. Machovič, Sorption of AsV on aluminosilicates treated with Fe(II) nanoparticles, *J. Colloid Interface Sci.*, 2006, **302**(2), 424–431.

14 A. Zehhaf, A. Benyoucef, C. Quijada, S. Taleb and E. Morallon, Algerian natural montmorillonites for arsenic (III) removal in aqueous solution, *Int. J. Environ. Sci. Technol.*, 2015, **12**(2), 595–602.

15 M. S. Hassan and H. M. Baioumy, Structural and chemical alteration of glauconite under progressive acid treatment, *Clays Clay Miner.*, 2006, **54**(4), 491–499.

16 D. Selby, U-Pb zircon geochronology of the Aptian/Albian boundary implies that the GL-O international glauconite standard is anomalously young, *Cretaceous Res.*, 2009, **30**(5), 1263–1267.

17 H. Moussout, H. Ahlafi, M. Aazza and C. El Akili, Performances of local chitosan and its nanocomposite 5% bentonite/chitosan in the removal of chromium ions (Cr(VI)) from wastewater, *Int. J. Biol. Macromol.*, 2018, **108**, 1063–1073.

18 Y. Zhou, B. Gao, A. R. Zimmerman, J. Fang, Y. Sun and X. Cao, Sorption of heavy metals on chitosan-modified biochars and its biological effects, *Chem. Eng. J.*, 2013, **231**, 512–518.

19 J. Yu, J. Zheng, Q. Lu, S. Yang, X. Zhang, X. Wang, *et al.*, Selective adsorption and reusability behavior for Pb^{2+} and Cd^{2+} on chitosan/poly(ethylene glycol)/poly(acrylic acid) adsorbent prepared by glow-discharge electrolysis plasma, *Colloid Polym. Sci.*, 2016, **294**(10), 1585–1598.

20 S. Zhang, Y. Dong, Z. Yang, W. Yang, J. Wu and C. Dong, Adsorption of pharmaceuticals on chitosan-based magnetic composite particles with core-brush topology, *Chem. Eng. J.*, 2016, **304**, 325–334.

21 M. Zhao, D. Wu, J. Chang, Z. Bai and K. Jiang, Synthesis of cup-like ZnO microcrystals via a CTAB-assisted hydrothermal route, *Mater. Chem. Phys.*, 2009, **117**(2–3), 422–424.

22 WEF AA, Standard Methods for the Examination of Water and Wastewater. *American Public Health Association*, AmericanWater Works Association, Water Environmental Federation, 21st edn, Washington DC, USA. 2005.

23 C. Jeon and W. H. Höll, Chemical modification of chitosan and equilibrium study for mercury ion removal, *Water Res.*, 2003, **37**(19), 4770–4780.

24 X.-j Hu, J.-s Wang, Y.-g Liu, X. Li, G.-m Zeng, Z.-l Bao, *et al.*, Adsorption of chromium (VI) by ethylenediamine-modified cross-linked magnetic chitosan resin: isotherms, kinetics and thermodynamics, *J. Hazard. Mater.*, 2011, **185**(1), 306–314.

25 D. Das and A. Pal, Adsolubilization phenomenon perceived in chitosan beads leading to a fast and enhanced malachite green removal, *Chem. Eng. J.*, 2016, **290**, 371–380.

26 R. Greenhalgh and J. Riley, The determination of fluorides in natural waters, with particular reference to sea water, *Anal. Chim. Acta*, 1961, **25**(2), 179–188.

27 O. A. Obijole, M. W. Gitari, P. G. Ndungu and A. Samie, Mechanochemically Activated Aluminosilicate Clay Soils and their Application for Defluoridation and Pathogen Removal from Groundwater, *Int. J. Environ. Res. Public Health*, 2019, **16**(4), 654.

28 A. Dada, A. Olalekan, A. Olatunya and O. Dada, Langmuir, Freundlich, Temkin and Dubinin–Radushkevich isotherms studies of equilibrium sorption of Zn^{2+} unto phosphoric acid modified rice husk, *IOSR J. Appl. Chem.*, 2012, **3**(1), 38–45.

29 J. Huggett and H. Petroclays, Time I, Space I, Dating A, Illite F. Minerals: Glauconites and Green Clays. *Reference Module in Earth Systems and Environmental Sciences*; Elsevier: Amsterdam, The Netherlands. 2013.

30 G. R. Thompson and J. Hower, The mineralogy of glauconite, *Clays Clay Miner.*, 1975, **23**(4), 289–300.

31 N. Antony, H. B. Sherine and S. Rajendran, Inhibition and biocide actions of sodium dodecyl sulfate-Zn^{2+} system for the corrosion of carbon steel in chloride solution, *Port. Electrochim. Acta*, 2010, **28**(1), 1–14.

32 D. Ramimoghadam, M. Hussein and Y. Taufiq-Yap, The effect of sodium dodecyl sulfate (SDS) and cetyltrimethylammonium bromide (CTAB) on the properties of ZnO synthesized by hydrothermal method, *Int. J. Mol. Sci.*, 2012, **13**(10), 13275–13293.

33 C. S. Sundaram, N. Viswanathan and S. Meenakshi, Uptake of fluoride by nano-hydroxyapatite/chitosan, a bioinorganic composite, *Bioresour. Technol.*, 2008, **99**(17), 8226–8230.

34 E. Srasra and M. Trabelsi-Ayedi, Textural properties of acid activated glauconite, *Appl. Clay Sci.*, 2000, **17**(1–2), 71–84.

35 M. Y. Nassar, I. S. Ahmed and M. A. Raya, A facile and tunable approach for synthesis of pure silica nanostructures from rice husk for the removal of ciprofloxacin drug from polluted aqueous solutions, *J. Mol. Liq.*, 2019, **282**, 251–263.

36 R. Singla, T. C. Alex and R. Kumar, On mechanical activation of glauconite: Physicochemical changes, alterations in cation exchange capacity and mechanisms, *Powder Technol.*, 2020, **360**, 337–351.

37 I. S. Ismael and S. Kharbish, Removing of as (V) from aqueous solution using natural and pretreated glauconite and halloysite, *Carpath. J. Earth Environ. Sci.*, 2013, **8**(1), 187–198.

38 A. S. Abdel-Bary, D. A. Tolan, M. Y. Nassar, T. Taketsugu and A. M. El-Nahas, Chitosan, magnetite, silicon dioxide, and graphene oxide nanocomposites: synthesis, characterization, efficiency as cisplatin drug delivery, and DFT calculations, *Int. J. Biol. Macromol.*, 2020, **154**, 621–633.

39 R. B. Nanjunda, L. V. Venkata, M. K. Vishnu, M. Mylarappa, N. Raghavendra and T. Venkatesh, Preparation of chitosan/different organomodified clay polymer nanocomposites: studies on morphological, swelling, thermal stability and anti-bacterial properties, *Nanosyst.: Phys., Chem., Math.*, 2016, **7**(4), 667–674.

40 N. Tazrouti and M. Amrani, Chromium (VI) adsorption onto activated kraft lignin produced from alfa grass (Stipa tenacissima), *BioResources*, 2009, **4**(2), 740–755.

41 X. Gao and J. Chorover, Adsorption of sodium dodecyl sulfate (SDS) at ZnSe and α-Fe_2O_3 surfaces: Combining infrared spectroscopy and batch uptake studies, *J. Colloid Interface Sci.*, 2010, **348**(1), 167–176.

42 R. B. Viana, A. B. F. da Silva and A. S. Pimentel, Infrared Spectroscopy of Anionic, Cationic, and Zwitterionic Surfactants, *J. Adv. Phys. Chem.*, 2012, **2012**, 903272.

43 L. Zhao and L. Gao, Coating multi-walled carbon nanotubes with zinc sulfide, *J. Mater. Chem.*, 2004, **14**(6), 1001–1004.

44 J. Guo, S. Chen, L. Liu, B. Li, P. Yang, L. Zhang, *et al.*, Adsorption of dye from wastewater using chitosan–CTAB modified bentonites, *J. Colloid Interface Sci.*, 2012, **382**(1), 61–66.

45 E. Günister, D. Pestreli, C. H. Ünlü, O. Atıcı and N. Güngör, Synthesis and characterization of chitosan-MMT biocomposite systems, *Carbohydr. Polym.*, 2007, **67**(3), 358–365.

46 M. Thommes, K. Kaneko, V. Neimark Alexander, P. Olivier James, F. Rodriguez-Reinoso, J. Rouquerol, *et al.*, Physisorption of gases, with special reference to the evaluation of surface area and pore size distribution (IUPAC Technical Report). *Pure and Applied Chemistry*, 2015. p. 1051.

47 K. A. Selim, R. S. El-Tawil and M. Rostom, Utilization of surface modified phyllosilicate mineral for heavy metals removal from aqueous solutions, *Egypt. J. Pet.*, 2018, **27**(3), 393–401.

48 L. D. Gidi, E. Z. Amare, H. A. Murthy and B. Abebe, Application of Novel Clay Composite Adsorbent for Fluoride Removal, *Mater. Sci. Res. India*, 2019, **16**(2), 164–173.

49 G. Karthikeyan, A. Shunmuga Sundarraj, S. Meenakshi and K. Elango, Adsorption dynamics and the effect of temperature of fluoride at alumina-solution interface, *J. Indian Chem. Soc.*, 2004, **81**(6), 461–466.

50 N. Hamdi and E. Srasra, Removal of fluoride from acidic wastewater by clay mineral: Effect of solid–liquid ratios, *Desalination*, 2007, **206**(1–3), 238–244.

51 A. Y. Dang-i, A. O. Boansi and M.-M. Pedevoah, Reduction of fluorine in water using clay mixed with hydroxyapatite, *International Journal of Applied Science and Technology*, 2015, **5**(2), 45–55.

52 M. Y. Nassar and M. Khatab, Cobalt ferrite nanoparticles *via* a template-free hydrothermal route as an efficient nano-adsorbent for potential textile dye removal, *RSC Adv.*, 2016, **6**(83), 79688–79705.

53 M. Y. Nassar, A. S. Amin, I. S. Ahmed and S. Abdallah, Sphere-like Mn_2O_3 nanoparticles: Facile hydrothermal synthesis and adsorption properties, *J. Taiwan Inst. Chem. Eng.*, 2016, **64**, 79–88.

54 M. Y. Nassar, M. M. Moustafa and M. M. Taha, Hydrothermal tuning of the morphology and particle size of hydrozincite nanoparticles using different counterions to produce nanosized ZnO as an efficient adsorbent for textile dye removal, *RSC Adv.*, 2016, **6**(48), 42180–42195.

55 Y.-S. Ho, Second-order kinetic model for the sorption of cadmium onto tree fern: A comparison of linear and non-linear methods, *Water Res.*, 2006, **40**(1), 119–125.

56 S. Lagergren, About the theory of so-called adsorption of soluble substances. Kunglia Svenska Vetenskapsakademiens, *Handlingar*, 1898, **24**(4), 1–39.

57 H. Yuh-Shan, Citation review of Lagergren kinetic rate equation on adsorption reactions, *Scientometrics*, 2004, **59**(1), 171–177.

58 W. J. Weber and J. C. Morris, *Proceedings of the International Conference on Water Pollution Symposium*, Pergamon Press, Oxford ; New York, Pergamon Press, 1962.

59 I. Langmuir, The Adsorption Of Gases On Plane Surfaces Of Glass, Mica And Platinum, *J. Am. Chem. Soc.*, 1918, **40**(9), 1361–1403.

60 H. Freundlich, Über die Adsorption in Lösungen, *Z. Phys. Chem.*, 1907, 385–470.

61 G. D. Halsey. The Role of Surface Heterogeneity in Adsorption, in: *Advances in Catalysis*, ed. W. G. Frankenburg VIK and Rideal E. K., Academic Press; 1952, vol. 4, pp. 259–269.

62 L. Ai, C. Zhang, F. Liao, Y. Wang, M. Li, L. Meng, *et al.*, Removal of methylene blue from aqueous solution with magnetite loaded multi-wall carbon nanotube: kinetic, isotherm and mechanism analysis, *J. Hazard. Mater.*, 2011, **198**, 282–290.

63 P. Zhang, I. Lo, D. O'Connor, S. Pehkonen, H. Cheng and D. Hou, High efficiency removal of methylene blue using SDS surface-modified $ZnFe_2O_4$ nanoparticles, *J. Colloid Interface Sci.*, 2017, **508**, 39–48.

64 M. Dubinin, The potential theory of adsorption of gases and vapors for adsorbents with energetically nonuniform surfaces, *Chem. Rev.*, 1960, **60**(2), 235–241.

65 M. S. Onyango, Y. Kojima, O. Aoyi, E. C. Bernardo and H. Matsuda, Adsorption equilibrium modeling and solution chemistry dependence of fluoride removal from water by trivalent-cation-exchanged zeolite F-9, *J. Colloid Interface Sci.*, 2004, **279**(2), 341–350.

66 M. Y. Nassar, I. S. Ahmed, T. Y. Mohamed and M. Khatab, A controlled, template-free, and hydrothermal synthesis route to sphere-like [small alpha]-Fe_2O_3 nanostructures for textile dye removal, *RSC Adv.*, 2016, **6**(24), 20001–20013.

67 H. N. Tran, S.-J. You, A. Hosseini-Bandegharaei and H.-P. Chao, Mistakes and inconsistencies regarding adsorption of contaminants from aqueous solutions: a critical review, *Water Res.*, 2017, **120**, 88–116.

68 R. Niwas, U. Gupta, A. A. Khan and K. G. Varshney, The adsorption of phosphamidon on the surface of styrene supported zirconium (IV) tungstophosphate: a thermodynamic study, *Colloids Surf., A*, 2000, **164**(2–3), 115–119.

69 S. K. Milonjić, A consideration of the correct calculation of thermodynamic parameters of adsorption, *J. Serb. Chem. Soc.*, 2007, **72**(12), 1363–1367.

70 N. Chen, Z. Zhang, C. Feng, M. Li, D. Zhu, R. Chen, *et al.*, An excellent fluoride sorption behavior of ceramic adsorbent, *J. Hazard. Mater.*, 2010, **183**(1–3), 460–465.

71 M. A. Kamal, S. Bibi, S. W. Bokhari, A. H. Siddique and T. Yasin, Synthesis and adsorptive characteristics of novel chitosan/graphene oxide nanocomposite for dye uptake, *React. Funct. Polym.*, 2017, **110**, 21–29.

72 R. Bhatt, B. Sreedhar and P. Padmaja, Adsorption of chromium from aqueous solutions using crosslinked chitosan–diethylenetriaminepentaacetic acid, *Int. J. Biol. Macromol.*, 2015, **74**, 458–466.

73 E. Saavedra-Labastida, M. C. Díaz-Nava, J. Illescas and C. Muro, Comparison of the Removal of an Anionic Dye from Aqueous Solutions by Adsorption with Organically Modified Clays and their Composites, *Water, Air, Soil Pollut.*, 2019, **230**(4), 88.

74 T. Bajda and Z. Kłapyta, Adsorption of chromate from aqueous solutions by HDTMA-modified clinoptilolite, glauconite and montmorillonite, *Appl. Clay Sci.*, 2013, **86**, 169–173.

75 S. Meenakshi, C. S. Sundaram and R. Sukumar, Enhanced fluoride sorption by mechanochemically activated kaolinites, *J. Hazard. Mater.*, 2008, **153**(1–2), 164–172.

76 Y. Zhang, X. Ying, C. Hao, L. Bingjie, G. Xiang, W. Dongfeng, *et al.*, La (III)-loaded bentonite/chitosan beads for defluoridation from aqueous solution, *J. Rare Earths*, 2014, **32**(5), 458–466.

77 G. Karthikeyan, A. Pius and G. Alagumuthu, Fluoride adsorption studies of montmorillonite clay, *Indian J. Chem. Technol.*, 2005, **12**, 263–273.

78 K. Pandi and N. Viswanathan, Remediation of Fluoride Using Montmorillonite@ Chitosan Biocomposite, *J. Chitin Chitosan Sci.*, 2015, **3**(1), 39–45.

79 J. Zhang, S. Xie and Y.-S. Ho, Removal of fluoride ions from aqueous solution using modified attapulgite as adsorbent, *J. Hazard. Mater.*, 2009, **165**(1–3), 218–222.